

2022-12-01

## Classification of Nuclear Pastas through Alpha Shapes Model

Daniela Ramirez Chavez  
*University of Texas at El Paso*

Follow this and additional works at: [https://scholarworks.utep.edu/open\\_etd](https://scholarworks.utep.edu/open_etd)



Part of the [Mathematics Commons](#), and the [Physics Commons](#)

---

### Recommended Citation

Ramirez Chavez, Daniela, "Classification of Nuclear Pastas through Alpha Shapes Model" (2022). *Open Access Theses & Dissertations*. 3716.

[https://scholarworks.utep.edu/open\\_etd/3716](https://scholarworks.utep.edu/open_etd/3716)

This is brought to you for free and open access by ScholarWorks@UTEP. It has been accepted for inclusion in Open Access Theses & Dissertations by an authorized administrator of ScholarWorks@UTEP. For more information, please contact [lweber@utep.edu](mailto:lweber@utep.edu).

CLASSIFICATION OF NUCLEAR PASTAS THROUGH ALPHA SHAPES MODEL

DANIELA RAMÍREZ CHÁVEZ

Master's Program in Physics

APPROVED:

---

Jorge A. López, Ph.D., Chair

---

Ravelo Ramon, Ph.D.

---

Art Duval, Ph.D.

---

Stephen Crites, Ph.D.  
Dean of the Graduate School

©Copyright

by

DANIELA RAMÍREZ CHÁVEZ

2022

CLASSIFICATION OF NUCLEAR PASTAS THROUGH ALPHA SHAPES MODEL

by

DANIELA RAMÍREZ CHÁVEZ, BS

THESIS

Presented to the Faculty of the Graduate School of

The University of Texas at El Paso

in Partial Fulfillment

of the Requirements

for the Degree of

MASTER OF SCIENCE

Department of Physics

THE UNIVERSITY OF TEXAS AT EL PASO

December 2022

# Acknowledgements

I would like to acknowledge my mentors for helping me throughout the project with their guidance and support. I would like to express my deepest appreciation and gratitude to Dr. Jorge López who generously provided knowledge and expertise and for his invaluable patience and feedback. This endeavor would not have been possible without Dr. Dmitriy Morozov, who introduced me into the mathematical model and the computational tools to analyze the nuclear data. I would like to extend my sincere thanks to Dr. Art Duval and Dr. Ramón Ravelo, my defense committee, for their support and knowledge. Special thanks to Jorge Munoz for giving me Cori hours to run the simulations. Lastly, I would like to mention Diana P. Carrasco-Rojas, Jacob A. Mireles Yahir E. Garay, Jahayra J. Chairez who helped me collecting the results.

# Abstract

The nuclear pasta is important because is an astromaterial with incredible strength that may be a source for gravitational waves, which observe from the rotation of neutron stars. The characterization of the pasta is vital because the nuclear phases have transport properties — compressibility, neutrino opacity, thermal conductivity, and electrical conductivity — associated with their shape for which neutron stars may be sensitive. These properties could interpret observations of supernova neutrinos, magnetic field decay, and crust cooling of accreting neutron stars. Here, we study the nuclear pasta using alpha shapes to achieve a phase characterization with the Minkowski functionals (area, volume, Euler characteristics, and curvature) where the principal analysis will revolve around the relation between the topological and geometry properties. The pasta phases are produced by means of molecular dynamics for nuclear matter systems with symmetrical properties (same quantity of protons and neutrons). The generated matter variates in density and final temperature, computing the pressure and energies for the time the system cools. Followed by calculating the Minkowski functionals using the alpha shapes model defined in the DIODE library for a fixed alpha radius. The use of alpha shapes give the result that the Minkowski functionals have a trend for a cooling system, and once the nuclear pasta achieves its final phase, their topological and geometric properties are associated with the density and temperature. We conclude that an optimized  $\alpha$  gives a clockwise trend in the Euler Characteristic *versus* Curvature graph, following gnocchi to anti-gnocchi pasta structures. Were found that the anti-pastas had an negative curvature, while the pastas were positive. As well, as long as the  $\alpha$  does not become a concave or convex hull the trend preserve with the exception of the lasagnas.

# Table of Contents

|  | Page |
|--|------|
| Acknowledgements . . . . .                                       | iv   |
| Abstract . . . . .   | v    |
| Table of Contents . . . . .                                      | vi   |
| List of Figures . . . . .  | viii |
| <b>Chapter</b>   |      |
| 1 Introduction . . . . .   | 1    |
| 2 Nuclear Pastas . . . . .                                       | 7    |
| 2.1 Nuclear Matter . . . . .                                     | 7    |
| 2.2 Properties of the Nuclear Pastas . . . . .                   | 9    |
| 2.3 Molecular Dynamics . . . . .                                 | 10   |
| 2.4 Methodology: LAMMPS . . . . .                                | 12   |
| 3 $\alpha$ - Shapes Method . . . . .                             | 15   |
| 3.1 Intersections of spheres of the order 1 and higher . . . . . | 17   |
| 3.2 Voronoi Diagram . . . . .                                    | 21   |
| 3.3 Minkowski functionals . . . . .                              | 23   |
| 3.3.1 Area . . . . .   | 23   |
| 3.3.2 Volume . . . . .   | 24   |
| 3.3.3 Euler Characteristic . . . . .                             | 24   |
| 3.3.4 Mean Curvature . . . . .                                   | 25   |
| 4 Results . . . . .  | 27   |
| 4.1 Nuclear Matter Structures . . . . .                          | 27   |
| 4.2 Minkowski Functionals . . . . .                              | 30   |
| 4.2.1 Dictate Level of Refinement . . . . .                      | 33   |
| 4.2.2 Relation $\chi$ , and $B$ . . . . .                        | 35   |

|   |   |    |
|---|---|----|
| 5 | Conclusions . . . . .                       | 38 |
|   | References . . . . .                        | 40 |
|   | <b>Appendix</b>                             |    |
| A | Results: Nuclear Pasta structures . . . . . | 44 |
| B | Table . . . . .                             | 48 |
|   | Curriculum Vitae . . . . .                  | 49 |



# List of Figures

|     |   |    |
|-----|---|----|
| 1.1 | Pasta structures formed in neutron star matter at densities $\rho = 0.08, 0.12,$<br>and $0.16 \text{ fm}^{-3}$ and at $T = 0.1 \text{ MeV}$ for a 5832-nucleon system with equal<br>number of protons and neutrons [1]. . . . .   | 1  |
| 1.2 | Neutron star layers zoom-in on the crust showing exotic pasta phases [18].  | 3  |
| 1.3 | Mélange of pasta structures as they vary with density. The values of the<br>density are given in $\text{fm}^{-3}$ and at $T = 0.1 \text{ MeV}$ for equal number of protons<br>and neutrons [4]. . . . .   | 4  |
| 2.1 | Theoretical predicted phase diagram for nuclear matter where the density is<br>given in multiples of normal nuclear matter density. For the EoS used, the<br>critical point is at $\rho_c = 0.061 \text{ fm}^{-3}$ and $T_c = 14.542 \text{ MeV}$ [35]. . . . .                                     | 8  |
| 2.2 | Schematic phase diagram for nuclear matter indicating the location of the<br>nuclear pastas in the density-temperature axes (with the density in units<br>of nuclear density). The third axis, “isospin”, is to represent the ratio of<br>protons to neutrons in the nuclear matter system. . . . . | 9  |
| 2.3 | Binding energy per nucleon for nuclear matter. [36] . . . . .   | 10 |
| 2.4 | Pasta structures obtained corresponding to the points “a” to “d” and “A”<br>to “D”. [36] . . . . .  | 11 |
| 2.5 | Curvature-Euler coordinates of the structures from figure 2.3. The lines<br>connect points with the same densities and temperatures varying from $T =$<br>$1.0 \text{ MeV}$ to $0.001 \text{ MeV}$ . [36] . . . . .   | 12 |
| 2.6 | Input file for $\rho = 0.02 \text{ fm}^{-3}$ for $T = 0.01 \text{ MeV}$ . . . . .   | 14 |
| 3.1 | Left panel: point set; middle panel: union of balls of radius $\alpha$ ; right panel:<br>Voronoi cells. . . . .   | 16 |

|      |  |    |
|------|--|----|
| 3.2  | Nerve composed of the intersection of the union of balls of radius $\alpha$ and the Voronoi cells. . . . .   | 16 |
| 3.3  | Lens description for $n=2$ . . . . .   | 18 |
| 3.4  | Calculate $V_{12}$ for $n = 2$ in terms of $V(R, \theta)$ and $S(R, \theta)$ . . . . .   | 19 |
| 3.5  | Sketch of intersections for $n=3$ . . . . .  | 20 |
| 3.6  | Process schematics to draw a Voronoi diagram with $n = 5$ , using the half-plane method. . . . .   | 21 |
| 3.7  | Procedure to define an $\alpha_n$ represented by $r_n$ . . . . .   | 22 |
| 3.8  | Defined simplexes for 3D objects. . . . .  | 23 |
| 4.1  | Nuclear matter structures for $T = 1$ MeV. . . . .   | 27 |
| 4.2  | Nuclear matter structures for $T = 0.50$ MeV. . . . .  | 28 |
| 4.3  | Energy and pressure as function of the temperature (leftmost) at $\rho = 0.05$ $\text{fm}^{-3}$ , and (rightmost) at $\rho=0.05, 0.08$ , and $0.12$ $\text{fm}^{-3}$ . . . . . | 29 |
| 4.4  | Diagram illustrating the comparison between two NM simulations. . . . .  | 30 |
| 4.5  | Minkowski functionals for $T = 1$ MeV with $0 < \alpha < 10$ , and density from $0.2$ to $0.2$ $\text{fm}^{-3}$ . . . . .  | 31 |
| 4.6  | Minkowski functionals for $T = 0.1$ MeV with $0 < \alpha < 10$ , and density from $0.2$ to $0.2$ $\text{fm}^{-3}$ . . . . .  | 32 |
| 4.7  | Volume normalization for $T = 0.01$ MeV . . . . .  | 33 |
| 4.8  | Illustration of the volume normalization, and $\chi$ for three optimizations of the $\alpha$ for $T = 0.25$ MeV. . . . .   | 34 |
| 4.9  | Euler Characteristic <i>versus</i> Curvature graph for optimized $\alpha$ . . . . .  | 35 |
| 4.10 | Euler-Curvature relation for (a-b) $\alpha = 1.5$ , and (c-d) $\alpha = 2.0$ . . . . .   | 37 |
| A.1  | Nuclear matter structures for $T = 0.01$ MeV. . . . .  | 44 |
| A.2  | Nuclear matter structures for $T = 0.25$ MeV. . . . .  | 45 |
| A.3  | Nuclear matter structures for $T = 0.50$ MeV. . . . .  | 46 |
| A.4  | Nuclear matter structures for $T = 0.75$ MeV. . . . .  | 47 |

|  |    |
|--|----|
| A.5 Nuclear matter structures for $T = 1$ MeV. . . . . | 47 |
|--|----|

# Chapter 1

## Introduction

The nuclear pastas are an exotic phase that could form in the inner crust of neutron stars, their name is associated to their resemblance to pasta-like shapes [1]. They are conformed by clusters of nucleons embedded in an electron gas [3]. The shapes of these structures are the result of the interaction between nuclear forces among protons and neutrons and the Coulomb forces between protons and electrons. Figure 1.1 shows an example of pastas found in the study of [1].

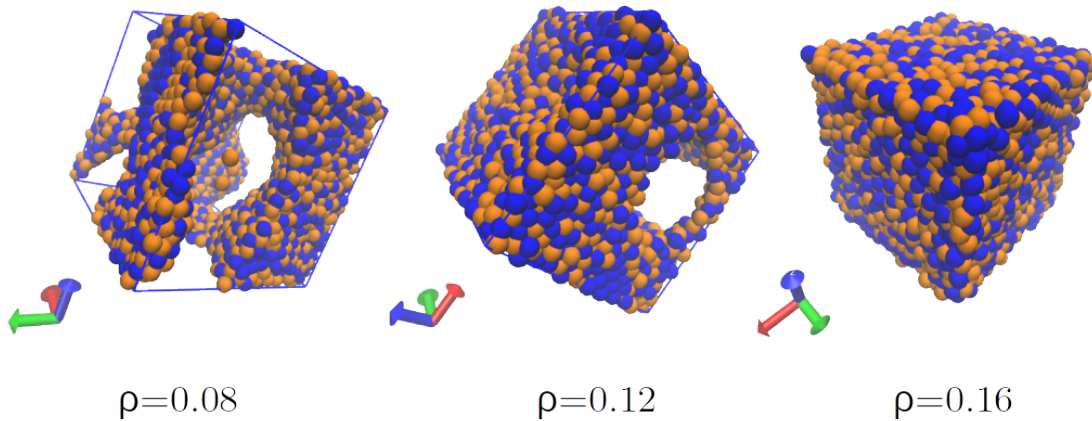


Figure 1.1: Pasta structures formed in neutron star matter at densities  $\rho = 0.08$ ,  $0.12$ , and  $0.16 \text{ fm}^{-3}$  and at  $T = 0.1 \text{ MeV}$  for a 5832-nucleon system with equal number of protons and neutrons [1].

It is expected that these pasta phases form in the crust of neutron stars [3]. Neutron stars are formed in core-collapse supernova explosions of a massive star. In such explosions, the consumption of its nuclear fuel bloats the star envelope followed by the ejection of mass [5], creating an unbalance between the thermal pressure and gravity, which contracts

the star [2, 5]. Throughout the process the star releases mass and, if the remaining mass surpasses the Chandrasekhar mass limit, the remnant will become a neutron star [1, 5].

The gravitational compression will be halted by the *nucleon degeneracy pressure* produced by the Pauli exclusion principle which forbids equal particles to occupy similar positions and energy levels. At such high pressures electrons are forced to combine with protons to generate matter consisting mostly of neutrons, thus giving the name of *neutron star* to the remnant of the dying star [5]. The reaction between electrons ( $e^-$ ) and protons ( $p$ ) that yields neutrons ( $n$ ) and electron neutrinos ( $\nu_e$ ) is known as *inverse beta decay*:



The production of neutrons is called *neutron drip* as neutrons begin to *drip* freely out of the structures they were in. It happens once the density is higher than a density of  $3.2 \times 10^{14}$   $\text{kg m}^{-3}$  [5].

In general, neutron stars have a mass between the Chandrasekhar limit,  $1.4M_\odot$  and a maximum mass of  $\sim 3M_\odot$ , a radius of  $\sim 10$  km, and an average density of  $6.65 \times 10^{17}$   $\text{kg m}^{-3}$  close to an average density of a degenerate Fermi gas composed of nucleons, or about that of normal nuclei [1, 2].

The inverse beta decay happens throughout the neutron star, reaching balances of neutron to protons to electrons of 8:1:1, but near the edge the proportion of protons increases considerably. The structure of the star consist of, basically, two regions: crust and core (Fig. 1.2). The crust has three layers; lighter mix layer, conformed of electron gas, protons and neutrons with densities decreasing practically to zero; neutron drip density layer, rich in neutrons with a density around  $4 \times 10^{14}$   $\text{kg m}^{-3}$ , and normal nuclear density layer around  $3 \times 10^{17}$   $\text{kg m}^{-3}$  [1].

At the densities and temperatures found in the crust of the neutron star, protons and neutrons form the structures known as pastas. The configuration of such structures vary according to the temperature and densities, Fig. 1.3 shows an instance of such variation, calculated with the model known as “Classical Molecular Dynamics” (CMD) [4]. It has

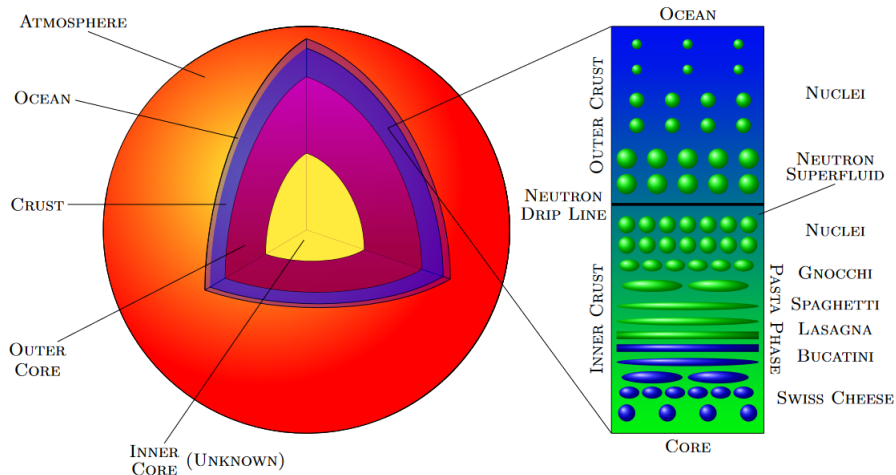


Figure 1.2: Neutron star layers zoom-in on the crust showing exotic pasta phases [18].

been found that the pasta occupies approximately 25% of the crust thickness and provides about 70% of the mass crust [20]. The pastas play an important role in the cooling of the neutron stars by regulating the flow of neutrinos, which constitute the main cooling mechanism.

Several models have been used to study the nuclear pastas, and they can be classified as static or dynamic models. The most common static models are the Compressible Liquid Drop Model, the extended Thomas-Fermi model, and the Hartree Fock method; while the dynamical models are the semi-classical molecular dynamics (CMD), and the quantum molecular dynamics (QMD) [4].

In particular the dynamical models follow the motion of either nucleons (CMD) or “quasi-particles” (QMD) at a given density and temperature as they interact by some prescribed force. CMD does this using classical newtonian mechanics, while QMD uses quantum mechanics. Although QMD is more proper as it respects all quantum principles, in practice uses a series of approximations that reduce its validity. Namely, the use of a few quasi-particles to represent the motions of groups nucleons, the use of average forces instead of nucleon-nucleon interactions, etc. produces systems that cannot form clusters nor produce the phase changes needed in the formation of the pastas.

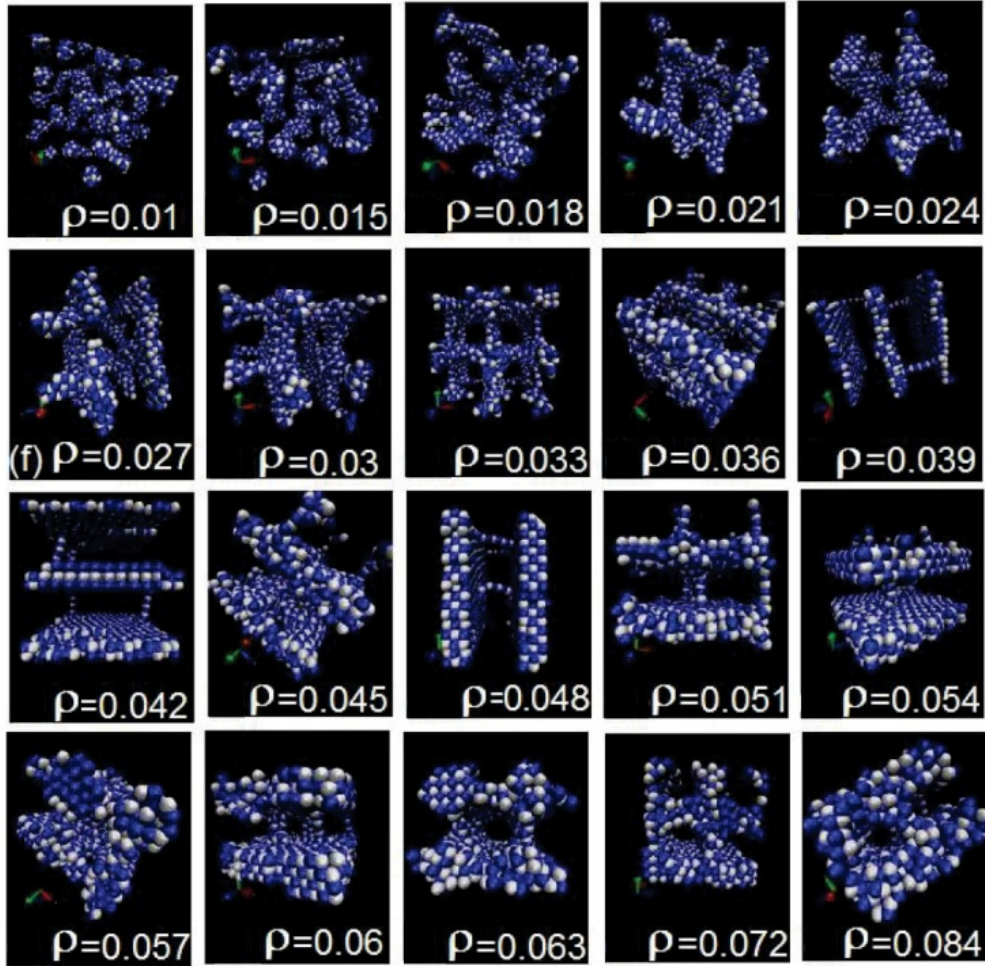


Figure 1.3: Mixture of pasta structures as they vary with density. The values of the density are given in  $fm^{-3}$  and at  $T = 0.1$  MeV for equal number of rotons and neutrons [4].

CMD, on the other hand, uses protons and neutrons as point particles and uses interaction potentials with forces that yield fragments and phase changes as it is needed in this type of study [4]. Additionally, CMD is computational cheaper compared to QMD and can be used to explore the phase space more thoroughly. This document uses CMD, and through the document it will be referred simply as molecular dynamics.

An important feature of the pastas is the characterization of their shapes as they vary as a function of density, temperature and proportion of protons to neutrons. The identification of phases has been done mainly globally using, for instance, average densities [24]

and volume fractions of the different phases [25], as well as bulk properties, such as the shear viscosity [26], diffusion coefficients [27], and radial correlation functions to characterize the nucleon distributions [28] and the pasta structure factor to study charge density fluctuations [29].

A major advance in this type of studies [4] used topological measures, such as the Minkowski functionals [30], to measure the superficial area, volume, mean curvature, and Euler characteristic of the pasta structures. Ever since, the Euler characteristic and mean curvature have been used to distinguish among the major pasta shapes, namely “lasagna”, “spaghetti”, “gnocci” and their anti-structures [1, 4, 31].

Although the study of Dorso, Giménez-Molinelli and L’opez [4] was selected to be showcased in “Physics” the magazine from the American Physical Society that reports on papers that “will change the course of research, inspire a new way of thinking, or spark curiosity”, it presented an impractical procedure.

A problem of the classification used is that it is based on solid bodies and not on a collection of points, such as those obtained by, e.g., CMD, and the construction of such solid bodies from a collection of points was based on the use of “voxels” representing a particle on a regular grid in three-dimensional space. Unfortunately, such procedure presented a major problem, namely, the size of the voxels is left unspecified, and had to be adjusted by the operator *by hand* on particle position data dumped by the code calculating the pasta structures. That is, it required manual interaction which made it difficult to be applied to vast amounts of data.

In a 2021 collaboration of LBNL’s researcher Dmitry Morozov and UTEP professor Jorge López and his group, a new method was developed and tested: the use of alpha shapes to substitute the voxels. The  $\alpha$ -shapes model has been used to measure structures as diverse as the morphology of mammalian baculum [32], . Moreover, the galaxy distribution of the Megaparsec Cosmic Web [33], and other. In this thesis the method will be used to test the relationship found between curvature and Euler characteristic in the classification of the pastas.



In this work nuclear pastas will be generated by a molecular dynamics simulator (LAMMPS), and the  $\alpha$ - shapes method will be used to obtain the solid structures from which the Minkowski functionals will be calculated. This procedure will be used to a plethora of structures obtained under different values of density, temperature and proton-neutron ratios. The various components of this procedure will now be presented in turn.

# Chapter 2

## Nuclear Pastas

This chapter focuses on the pasta phase caused by nucleon interactions in nuclear matter, that is, neglecting the electron gas interaction. It will describe the pasta as part of the phase diagram of nuclear matter, will explain how to study it using molecular dynamics with the so-called “New Medium potential”.

### 2.1 Nuclear Matter

Although it was argued that the pastas are formed due to the interplay of nuclear and Coulomb forces, pastas can also form from the competition of the neutron-proton attraction and the proton-proton and neutron-neutron repulsion, i.e. without the electron gas. As studied in [1], the main effect of an embedding electron gas on the pastas is in the distribution of cluster size. In this section we study nuclear matter, which differs from the neutron star matter, where the electron gas fills the voids of the clusters in the nuclear pastas, whereas for nuclear matter the voids remain empty. Nuclear pastas are the low density-low temperature limit of nuclear matter.

Systems composed solely of protons and neutrons (with no embedding electrons) are known as nuclear matter. Being fermions, at low densities a gas of protons and neutrons can be approximated as a free Fermi gas in which the particles interact with one another only through the exclusion principle embedded in the Fermi Dirac statistics. At higher densities, however, the strong and Coulomb forces play an important role, and the effects of the interactions must be added. Since such interaction has not been yet evaluated from first principles (e.g. QCD and the like), phenomenological methods must be used.

The usual approach is to use a phenomenology-inspired interaction in the form of a mean field (for QMD or static computational methods) or a two-body potential (for CMD). Such interactions are adjusted as to yield known properties of nuclei, such as the energy per nucleon in infinite systems ( $\varepsilon(n_0) = -8$  MeV) and saturation density ( $n_0 = 0.16$   $fm^{-3}$ ) and  $T = 0$ . Also, since a nucleus is stable at this density, the pressure should be  $p = 0$ , and, as observed in experiments of nuclear oscillations, the compressibility should be of the order  $100 \text{ MeV} < K(n_0) < 300 \text{ MeV}$  [34].

These basic ingredients are enough to deduce that nuclear matter can exist in gaseous and liquid states, as well as in a mixture of gas and liquid in a coexistence region. Figure 2.1 shows the phase diagram of nuclear matter obtained for a phenomenological interaction [34].

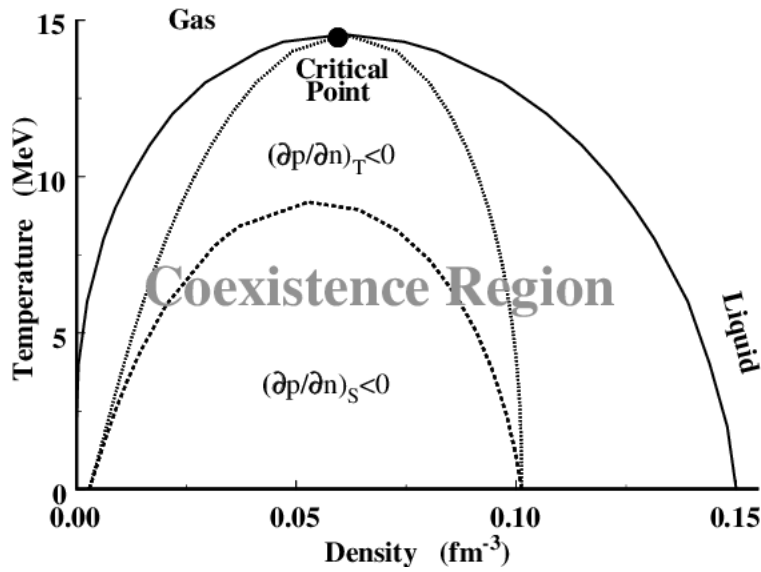


Figure 2.1: Theoretical predicted phase diagram for nuclear matter where the density is given in multiples of normal nuclear matter density. For the EoS used, the critical point is at  $\rho_c = 0.061$   $fm^{-3}$  and  $T_c = 14.542$  MeV [35].

## 2.2 Properties of the Nuclear Pastas

In spite of how detailed the phase diagram 2.1 is, it is missing the phases that occur at very low temperatures (under  $T = 1.0$  MeV) and sub-saturation densities ( $< 0.16 \text{ fm}^{-3}$ ), i.e. the pasta phases. Schematically, the nuclear pasta exists in the lower part of the diagram shown in figure 2.2. Shown in figure 2.2, is a third variable, isospin, which represents the proton fraction

$$\rho = \frac{z}{A} \tag{2.1}$$

where  $z$  is the number of protons and  $A$  is number of nucleons and it equals  $n + p$ .

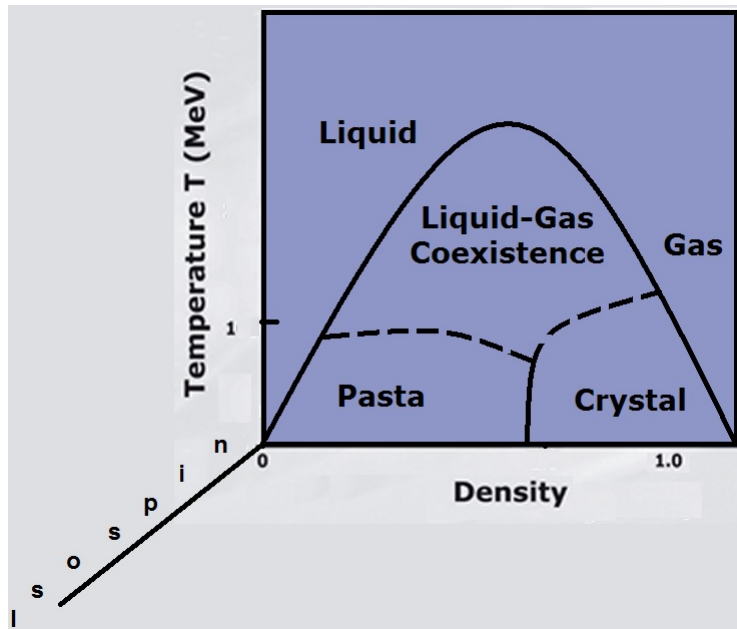


Figure 2.2: Schematic phase diagram for nuclear matter indicating the location of the nuclear pastas in the density-temperature axes (with the density in units of nuclear density). The third axis, “isospin”, is to represent the ratio of protons to neutrons in the nuclear matter system.

Previous studies with various interaction potentials have investigated the structure of nuclear matter at various densities and temperatures. Figure 2.3 shows the binding energy per nucleon at several densities and temperatures.

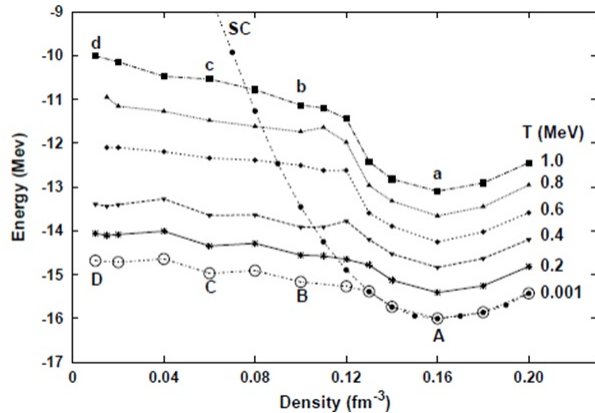


Figure 2.3: Binding energy per nucleon for nuclear matter. [36]

Such plot, from [36], shows that at densities around  $0.16 \text{ fm}^3$  the curves follow the “U” shape characteristic of a uniform crystalline phase, with the minimum of the “U” corresponding to the normal nuclear density ( $0.16 \text{ fm}^{-3}$ ), known as saturation density. Notice that if the density decreases below, say,  $0.13 \text{ fm}^3$ , the systems move away from the uniform phase forming non-homogeneous stable arrangements, known as the pasta phase. Figure 2.4 shows the structures obtained at  $T = 0.001 \text{ MeV}$  and at  $T = 1.0 \text{ MeV}$  for the four densities labeled from “a” to “d”, and “A” to “D”.

In preparation to the upcoming section on the Minkowsly functionals, it is convenient to show the location of the structures presented in figures 2.3 and 2.4 in the Curvature-Euler number plane. Figure 2.5Curvature-Euler shows the trajectories of the cooling of such structures as they vary from  $T = 1.0 \text{ MeV}$  to  $0.001 \text{ MeV}$  [36]. It is easy to see the value of the plane Curvature-Euler number in the characterization of the pastas.

## 2.3 Molecular Dynamics

In a nutshell, CMD treats nucleons as classical particles interacting through pair potentials and predicts their dynamics by solving their equations of motion numerically. The method does not contain adjustable parameters, and uses the Pandharipande potentials [32], or

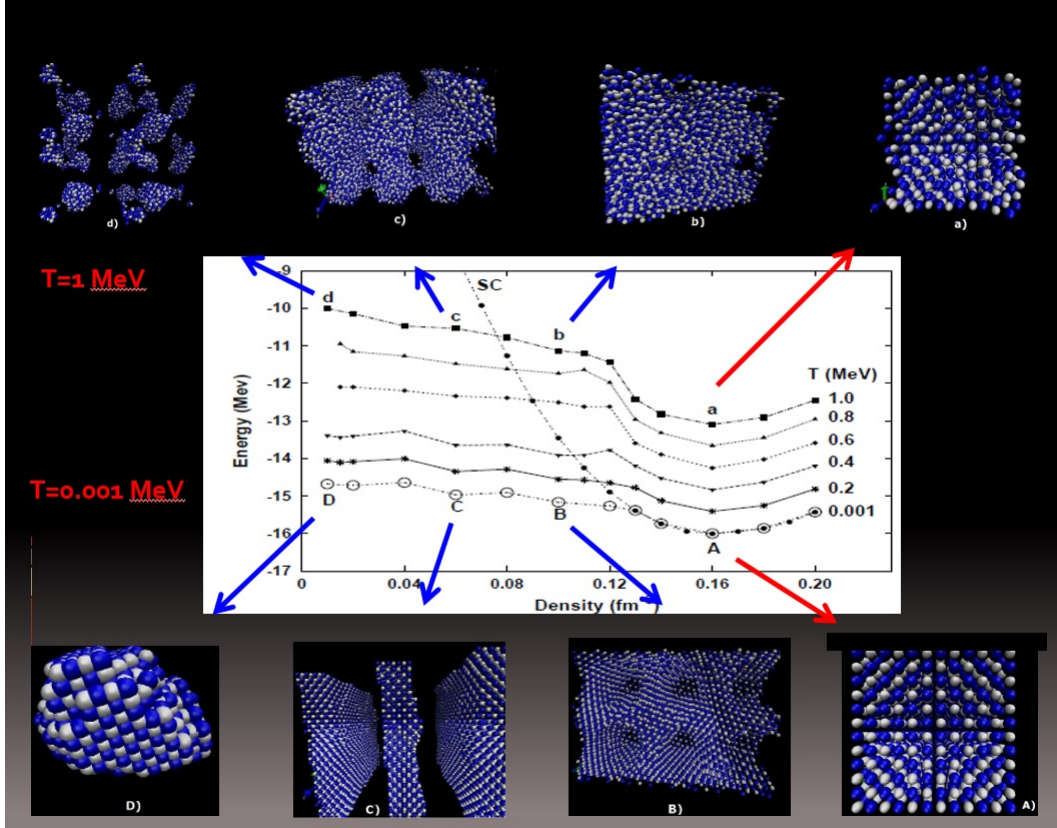


Figure 2.4: Pasta structures obtained corresponding to the points “a” to “d” and “A” to “D”. [36]

the “New Medium Potential”, which is a fine tuning of the previous one. These potentials have an attractive term between neutrons and protons, and a repulsive one between equal nucleons. The New Medium Potential is given by the following expressions:

$$\begin{aligned}
 V_{np}(r) &= \frac{V_r}{r}^{-\mu_r r} - \frac{V_r}{r_c}^{-\mu_r r_c} - \frac{V_a}{r}^{-\mu_a r} + \frac{V_a}{r_c}^{-\mu_r r_c} \\
 V_{nn}(r) &= \frac{V_0}{r}^{-\mu_0 r} - \frac{V_0}{r_c}^{-\mu_0 r_c}
 \end{aligned}
 \tag{2.2}$$

where  $r_c$  is the cutoff radius after which the potentials are set to zero (table 2.1). The potential does not include the Coulomb potential reducing to a nucleon environment.

These potentials attain a saturation density of  $0.16 \text{ fm}^{-3}$ , a binding energy at saturation

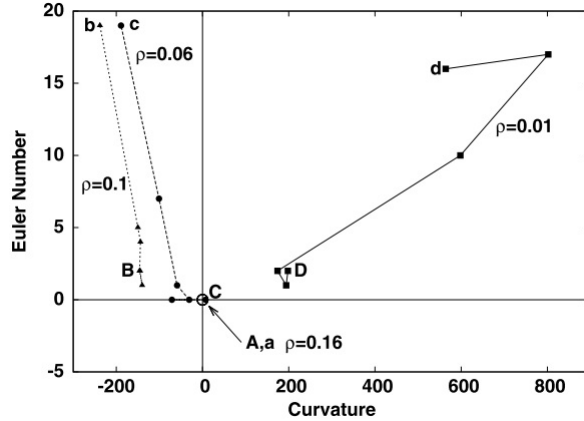


Figure 2.5: Curvature-Euler coordinates of the structures from figure 2.3. The lines connect points with the same densities and temperatures varying from  $T = 1.0$  MeV to 0.001 MeV. [36]

density and  $T = 0$  of  $E = -16$  MeV/nucleon and a compressibility about 250 MeV [1].

## 2.4 Methodology: LAMMPS

The molecular dynamics calculations are performed using the code LAMMPS from Sandia National Lab [16] operating with a force table obtained from the New Medium Potential. The procedure is to place a large number of protons and neutrons in a cubic cell with its size adjusted to have a desired density by means of  $\rho = \frac{N+Z}{l^3}$ . Such cell is then surrounded by replicas to simulate periodic boundary conditions. In the beginning, the particles are endowed with velocities corresponding to a Maxwell-Boltzmann distribution at an initial temperature, and the system is then cooled down from a relatively high temperature ( $T \leq 4.0$  MeV) to a desired cool temperature in small temperature steps ( $\Delta T = 0.01$  MeV) and assuring that the energy, temperature, and their fluctuations are stable.

The template text file to simulate the nuclear matter is shown in the figure 2.6. Each simulation was contained in a box with dimensions to hold 4000 nucleons with densities ranging from  $0.2 \text{ fm}^{-3} < \rho < 0.20 \text{ fm}^{-3}$ .

Table 2.1: Parameter set for the CMD computations [1].

| Parameter | Pandharipande | New Medium | Units            |
|-----------|---------------|------------|------------------|
| $V_r$     | 3088.118      | 3097.0     | MeV              |
| $V_a$     | 2666.647      | 2696.0     | MeV              |
| $V_0$     | 373.118       | 379.5      | MeV              |
| $\mu_r$   | 1.7468        | 1.648      | fm <sup>-1</sup> |
| $\mu_a$   | 1.6000        | 1.528      | fm <sup>-1</sup> |
| $\mu_0$   | 1.5000        | 1.628      | fm <sup>-1</sup> |
| $r_c$     | 5.4           | 5.4/20     | fm               |

In detail, the nuclear pastas were cooled down from 4 MeV to the final temperatures 0.01, 0.25, 0.50, 0.75, and 1 MeV by taking 10 snapshots of the kinetic and potential energy, the pressure, and the temperature at that moment. The snapshots are controlled by the command line dump (fig. 2.6) and the run command. In the command line dump, LAMMPS stores information in lammpstrj format every 100,000 timesteps. For the nuclear pastas, the position of the particles with their respective velocity was stored. Whereas the run command defines the number of cycles in each timestep, by establishing that a timestep is a differential time in seconds of a computer step with the subsequent step. Implying the input file runs one million cycles every 0.10 timesteps when the nuclear structure is cooling down.

Furthermore, the temperatures are fixed to one particle type from 4 MeV to  $\Delta T$  during a run with the nvt command. The code is also limited by the pair coeff commands, in which a particle interaction potential is limited by the distance depending of the particle's ID(fig. 2.6) For the simulations, the algorithm used was Hessian-free truncated Newton algorithm. Where, at each iteration of the quadratic model, the energy potential is solved by a conjugate gradient inner iteration [16].

The temperature is calculated through the kinetic energy divided by the degrees of



```

input_T4_01D02x5 - Notepad
File Edit Format View Help
#Nuclear mode: NSM (Nuclear star matter)
#this requires ../newmed.table
# p = 0.02 fm^-3, x = 0.5, T = 4->0.01 MeV
#-----Initialize simulation-----
units          lj #unitless lennard-jones
atom_style     atomic #coarse-grain liquids, solids, metals
timestep       0.10
region         box block 0 58.48 0 58.48 0 58.48 #distance fm
create_box     2 box # no. atomtypes, region
mass           1 938 # protons MeV
mass           2 938 # neutrons MeV (together nucleons)
#-----Create Atoms-----
create_atoms   2 random 2000 1234 box
create_atoms   1 random 2000 5678 box #total 4000nucleons
#-----Define Interatomic Potential-----
pair_style     table linear 5000 #doc type
neighbor       1.2 bin #default
neigh_modify   every 1 delay 0 check yes one 8000 page 80000
thermo_style   custom step temp ke epair etotal press cpu
thermo         20000
pair_coeff      1 1 ../newmed.table NN 5.4
pair_coeff      1 2 ../newmed.table NP 5.4
pair_coeff      2 2 ../newmed.table PP 20.0
#-----Run Minimization-----
min_style      hftn
minimize       0 1.0 1000 100000
velocity       all create 4.0 1776
#-----create dump file: cfg,lampstrj-----
dump myDUMP all custom 100000 output_T4_01D02x5.lampstrj id type x y z vx vy vz
fix 1 all nvt temp 4.0 0.01 100.0 # MeV
run 1000000
Ln 32, Col 1      100%  Unix (LF)      UTF-8

```

Figure 2.6: Input file for  $\rho = 0.02 \text{ fm}^3$  for  $T = 0.01 \text{ MeV}$ .

freedom. By observing that the kinetic energy is associated with the momentum, there are two approaches to calculating the thermal velocity from the total velocity: thermostating or barostatting. The nuclear pastas needed the thermostating approach because the temperature is controlled for one type of particle and used Nosee-Hover Thermostats from several. In other words, the method equilibrates the system through the temperature, not the pressure.

The Nosee-Hover Thermostats only collect the translational velocity of the particles. And it performs a time integration, which means that it predicts the next position of the particle with the potential and from the velocity, calculates the kinetic energy, and extracts the temperature without adding extra temperature to the system like in other thermostats. Not performing time integration updates.

The computations were performed in the HPC system NERSC of LBNL [37], and once they were finished the output files containing the position and velocities of each of the particles were imported to be used in a visualization code [38] to picture the pastas.

# Chapter 3

## $\alpha$ - Shapes Method

The problem of obtaining a solid object out of a set of points distributed in 3 dimensions has been approached in mathematics mainly by the Delaunay triangulation. In this method, a triangulation mesh is created for a given set of discrete points, such that no point of the set is inside of any circumscribed sphere of any triangle, that is the circumscribed spheres of every triangle have empty interiors [8].

It is worth mentioning that the Delaunay triangulation is not unique for a given set of points, but it is useful in producing solid bodies that encompass a cloud of points, from which a volume, surface area, average curvature and Euler characteristic can be computed.

Later, the triangles of Delaunay were generalized to simplicial complexes, that is, sets of points, line segments, triangles, and higher dimensional counterparts, into what was named the “Alpha shapes” method. The name arises from the use of  $\alpha$  as a parameter to characterize the simplicial complexes, which have vertices in the point set, simplices on the Delaunay triangles, and even different weights for the points; this makes the alpha complexes efficiently computable [9].

The alpha shapes method has been used extensively in applications ranging from macromolecules [10], where atoms are weighted points, to the reconstruction of surfaces off sampled points [11]. These advances have been facilitated by the creation efficient algorithms [12, 14].

To explain the alpha shapes method in simple terms, we use the example of D. Morozov [13]. The guiding idea is to determine the volume of a set of points. Figure 3.1 shows a set of points,  $P$ , in its left panel. To create a volume (or an area in 2 dimensions) corresponding to the set of points, one can place spheres,  $B_\alpha(p)$ , of radius  $\alpha$  centered at each

point, and take the volume of the union of the spheres,  $U_{balls,\alpha} = \bigcup_p B_\alpha(p)$ , as the volume of the set; this is represented in the middle panel of figure 3.1. To avoid overcounting due to the overlap of the spheres, one resorts to the use of the Voronoi diagram which partitions the space between points by bisecting them:  $Vor(p) = \{x \in R^n \mid \|x - p\| \leq \|x - q\| \forall q \in P\}$ ; its application to the point set of the figure 3.1 is shown in the right panel of the figure.

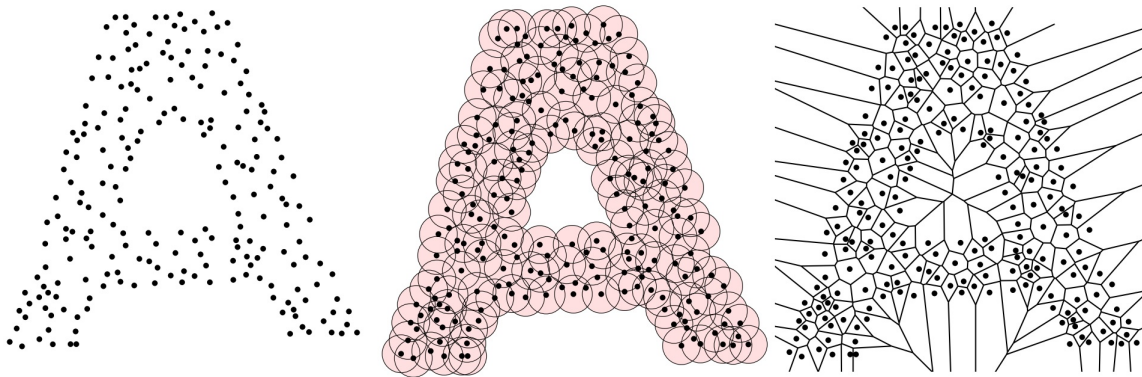


Figure 3.1: Left panel: point set; middle panel: union of balls of radius  $\alpha$ ; right panel: Voronoi cells.

Finally, to limit the Voronoi cells that extend to infinity one forms the intersection of the union of balls and Voronoi cells, thus forming the nerve  $\mathcal{C} = \{B_\alpha(p) \cap Vor(p)\}$ . The results is shown in figure 3.2.

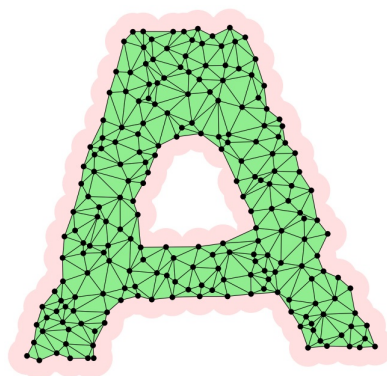


Figure 3.2: Nerve composed of the intersection of the union of balls of radius  $\alpha$  and the Voronoi cells.

Next we present the alpha shapes method and its use to extract the Minkowski functionals to characterize the pasta.

### 3.1 Intersections of spheres of the order 1 and higher

Here we will introduce the intersection of spheres with the consideration that in some arrangements, some spheres may have one point overlap, the intersection of  $m$  spheres, or even non-interacting spheres. Next, the implications of the Voronoi Diagram are followed by calculating the Euler characteristic and curvature.

The method depends on the number of spheres ( $n$ ) intersecting among each other. For  $n = 1$ , the volume ( $V$ ) and superficial area ( $S$ ) of the sphere are calculated with the following equations,

$$V_d(R) = \frac{\pi^{2/d}}{\Gamma(\frac{d}{2} + 1)} R^d, d \geq 1 \tag{3.1}$$

$$S_d(R) = d \frac{\pi^{2/d}}{\Gamma(\frac{d}{2} + 1)} R^{d-1}, d \geq 2 \tag{3.2}$$

Where  $d$  is the dimension's degree,  $R$  is the sphere radius. The proof of these equations is given via the summation of the volumes  $E^{(d-1)}$  [15].

For a system with  $n = 2$ , the intersection of the spheres must be analyzed before calculating the area and volume. Assume that sphere one,  $n_1$ , has a radius  $R_1$  and is centered at  $c_1$ , while the second sphere,  $n_2$ , has a radius  $R_2$  and is centered at  $c_2$ . The arrangement of the spheres could lead to an empty space, one point intersection, a lens, or  $c_1$  inside  $c_2$  or *vice versa* (fig. 3.3).

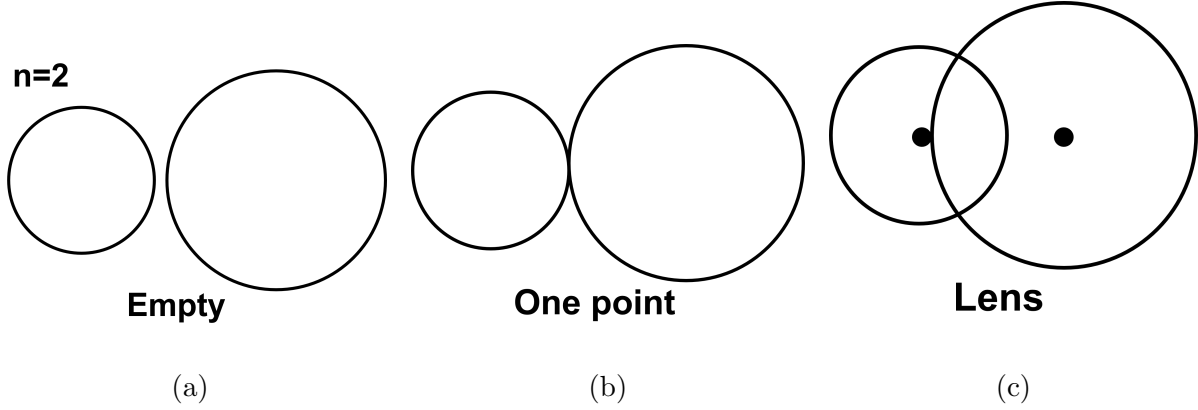


Figure 3.3: Type of intersections for  $n=2$ .

The type of intersection determines the method to calculate  $V$  and  $S$ , the empty case (fig. 3.3a) and one point intersection (fig. 3.3b) use invariably equations 3.1-3.2; however, for the lens case (fig. 3.3c), the overlap area and volume must be subtracted from the volume and surface of  $n_1$  and  $n_2$ . The  $V$  and  $S$  of the total system are thereby calculated with

$$V = V_1 + V_2 - V_{12}, \quad (3.3)$$

$$S = S_1 + S_2 - S_{12}, \quad (3.4)$$

where  $V_{12}$  and  $S_{12}$  are unions. The above equations include the overlap region, which essentially is a lens, and these exist when:

$$|R_1 - R_2| \leq \|c_2 - c_1\| \leq |R_1 + R_2|, \quad (3.5)$$

The calculation of the overlap region cannot be written in terms of equations 3.1-3.2 instead these should be arranged in terms of the angles  $\theta_1$  and  $\theta_2$  and the intersection point,  $t_{12}$  (fig. 3.4).

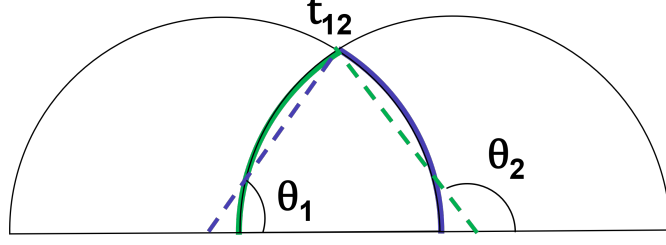


Figure 3.4: Calculate  $V_{12}$  for  $n = 2$  in terms of  $V(R, \theta)$  and  $S(R, \theta)$ .

Changing to polar coordinates, the lens region for 3D is solved with,

$$V_3(R, \theta) = \frac{\pi R^3}{3} (1 - \cos\theta)^2 (2 + \cos\theta), \quad (3.6)$$

$$S_3(R, \theta) = 2\pi R^2 (1 - \cos\theta), \quad (3.7)$$

where  $\theta$  takes values in  $[0, \pi]$ . However, from these equations, the angles are unknown, which can be found by knowing  $t_{12}$ ,

$$t_{12} = \left(\frac{c_1 + c_2}{2}\right) + \frac{R_1^2 - R_2^2}{\|c_2 - c_1\|^2} \left(\frac{c_2 - c_1}{2}\right) \quad (3.8)$$

$$\|t_{12} - c_1\| = \frac{1}{2} \left( \|c_2 - c_1\| + \frac{R_1^2 - R_2^2}{\|c_2 - c_1\|} \right) \quad (3.9)$$

$$\|t_{12} - c_2\| = \frac{1}{2} \left( \|c_2 - c_1\| + \frac{R_2^2 - R_1^2}{\|c_2 - c_1\|} \right) \quad (3.10)$$

where the transposed vector  $t'_{12}$  of the intersection lens  $t_{12}$  defines  $\|t_{12}\|^2 = t'_{12} t_{12}$  [15]. Hereafter, with Pythagorean theorem calculate, (fig. 3.4),

$$|\cos \theta_1| = \frac{\|t_{12} - c_1\|}{R_1} \quad (3.11)$$

$$|\cos \theta_2| = \frac{\|t_{12} - c_2\|}{R_2}. \quad (3.12)$$

Once the angles are known plug them in equations 3.6 - 3.7. Notice that for a fixed  $\alpha$  radius, where all the spheres have the same radius, the above equations reduce to  $\theta_1 = \theta_2$ .

Increasing the number of spheres to  $n = 3$  gives a variety of arranged systems, *i.e.* no contact point, 2-6 contact points. This leads to a region that is subtracted twice ( $S_{123}$  and  $V_{123}$ ) and must be added to the net sum. It is because after the second sphere, for  $n_3$  the subtraction with respect  $n_1$ , and  $n_2$  overlaps in the region  $S_{123}$  (fig. 3.5).

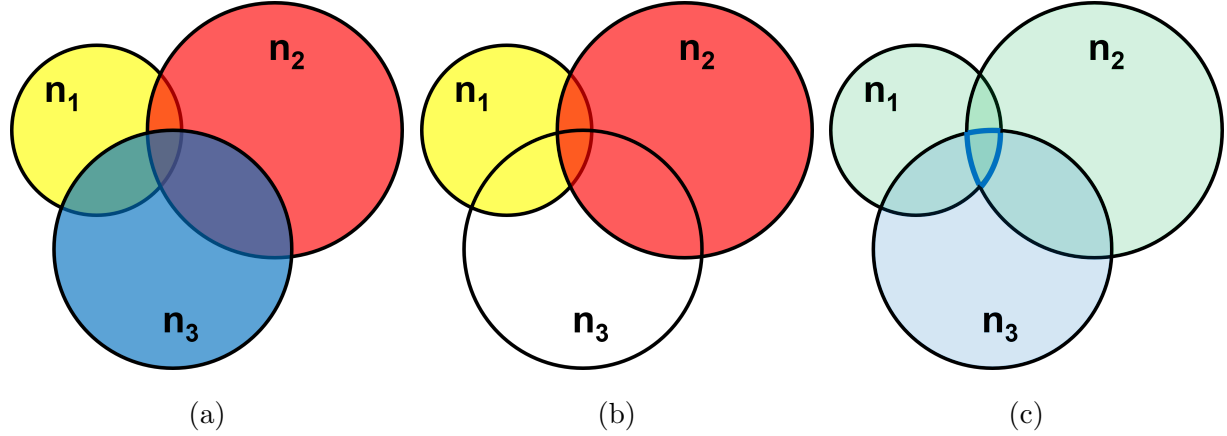


Figure 3.5: Sketch of intersections for  $n=3$ . (a) Shows the sum of  $S_1$ ,  $S_2$  and  $S_3$ , (b) the union in between  $n_1$  and  $n_2$ , and (c) highlights the overlap region  $S_{123}$ .

Then, the total  $V$  and  $S$  is written as

$$V = V_1 + V_2 + V_3 - V_{12} - V_{13} - V_{23} + V_{123} \quad (3.13)$$

$$S = S_1 + S_2 + S_3 - S_{12} - S_{13} - S_{23} + S_{123} \quad (3.14)$$

where the union  $n_1$ ,  $n_2$  and  $n_3$  is trivial [15]. With the previous knowledge, it is noticeable that when the quantity of spheres increases, the union of spheres will be subtracted from the summation. If a triple union exists, this will be added to the system. A general expression higher order intersections are given as,

$$V = \sum_{1 \leq i \leq n} V_i - \sum_{1 \leq i_1 \leq i_2 \leq n} V_{i_1 i_2} + \sum_{1 \leq i_1 \leq i_2 \leq i_3 \leq n} V_{i_1 i_2 i_3} + \dots + (-1)^{n-1} V_{i_1 i_2 \dots i_n} \quad (3.15)$$

$$S = \sum_{1 \leq i \leq n} S_i - \sum_{1 \leq i_1 \leq i_2 \leq n} S_{i_1 i_2} + \sum_{1 \leq i_1 \leq i_2 \leq i_3 \leq n} S_{i_1 i_2 i_3} + \cdots + (-1)^{n-1} S_{i_1 i_2 \cdots i_n} \quad (3.16)$$

These expressions indicate the volume and surface area of the intersections of spheres; however, for practical computations, the location of  $c_n$ , data position, with its nearest neighbors requires locating them in a narrowed region instead of the complete space.

## 3.2 Voronoi Diagram

Once the number of data points increases ( $c_n$  for  $n = 1, 2, 3, \dots, N$ ), the complexity to identify the closest  $c$  to a point  $q$  increases too. Therefore, a technique like the Voronoi diagram simplifies the complexity of measuring the intersection for nearest neighbors. To design this diagram, one must draw planes at half the distance of  $c$  to another. The intersections of these planes define a Voronoi cell for  $c_n$  point. The Voronoi cell defines the region closest to a point  $c$ , *e.g.*, if  $q$  is located in the cell that contains  $c_3$ , then  $q$  is closer to  $c_3$  than any other point  $c$  (fig. 3.6).

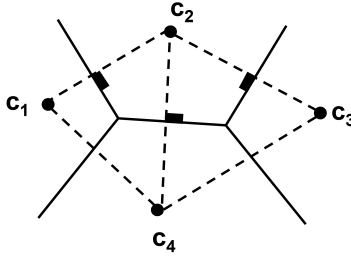


Figure 3.6: Process schematics to draw a Voronoi diagram with  $n = 5$ , using the half-plane method.

In other words, the Voronoi cell is constrained by the location of point  $q$ . If  $q$  is moved out of the cell, it will belong to another cell, and the point is renamed to  $p$ . Hence, the Voronoi diagram is the limit where  $q$  and  $p$  have the equivalent distance to their respective  $c_n$ . Which is described by the equation,



$$Vor(p) = \{x \in R^n \mid \|x - p\| \leq \|x - q\| \forall q \in P\} \quad (3.17)$$

Followed by the selection of the fixed  $\alpha$ , the next step is to draw a sphere for each vertex (particles' position) where the Voronoi diagram identifies which particle lands inside the sphere of a neighboring cell (fig. 3.7).

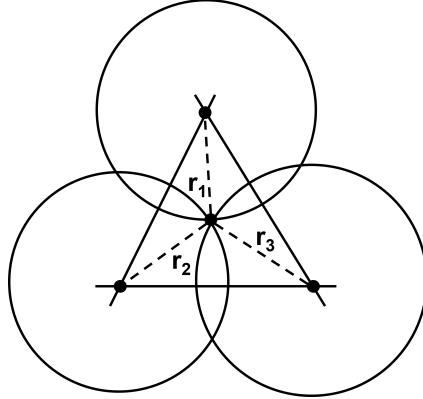


Figure 3.7: Procedure to define an  $\alpha_n$  represented by  $r_n$

The Voronoi diagram creates a skeleton that connects the nearest data points. This skeleton is conformed of vertexes, edges, triangles, and tetrahedrons for a structure in 3D. A vertex is a particle isolated from others where the distance that separates it is greater than the  $\alpha$  radius. The interaction of two data points defines an edge, and its name is associated with the fact that when two data points interact, these create an edge on the skeleton similar to a tail. The triangle defines the interaction of three particles, and these mostly represent the superficial area of the structure. Finally, the tetrahedron will determine the volume of the nuclear structure formed by the interaction of three particles (fig. 3.8). The complexity of particles interacting in the Voronoi diagram defines the simplex degree. For example, a simplex of degree 0 is a vertex, degree 1 is an edge, degree 2 is a triangle, and degree 3 is a tetrahedron. From these simplexes, the spheres with an  $\alpha$  radius will be drawn centered on the particle's position from the nuclear matter structures, and the Minkowski functionals are calculated with the intersection of spheres.

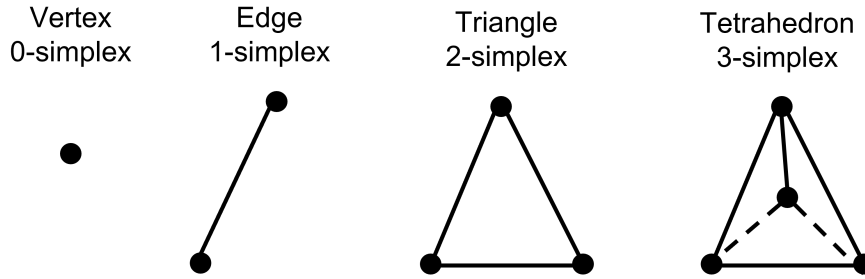


Figure 3.8: Defined simplexes for 3D objects.

The application of the  $\alpha$ -shapes model was added with the DioDe library from Dmitriy Morozov, which works on python. This library reads the particle positions of the molecular dynamics simulations and calculates the simplexes found with their respective lengths. However, not all the simplexes given satisfy the desired conditions. For instance, the lengths must be proportional to the chosen  $\alpha$ , and only the simplex-2 and simplex-3 are required to compute the Minkowski functionals.

### 3.3 Minkowski functionals

Once the  $\alpha$ -shapes model is implemented to calculate the simplexes of the nuclear structure, the next step is to get the Minkowski functionals. It is the geometrical and topological properties calculated from a structure, and it calculates the superficial area( $S$ ), volume( $V$ ), Euler characteristic ( $\chi$ ), and curvature ( $B$ ).

#### 3.3.1 Area

The acquisition of the area requires simplex-2 (triangle), which determines the superficial area of the nuclear structure, and a fixed  $\alpha$ . DioDe gives vectors for the positions of the particles, then to calculate the area,

$$S = \frac{1}{2} \|(\vec{B} - \vec{A}) \times (\vec{C} - \vec{A})\| \quad (3.18)$$

where  $\vec{A}$ ,  $\vec{B}$ ,  $\vec{C}$  are the vectors given of the simplex-2. Apply this function to every simplex-2 and add them.

### 3.3.2 Volume

The volume calculation can be obtained with the parallelepiped area, filled with six tetrahedrons. Then,

$$V_{tet} = \frac{1}{6}(\vec{l}_1 \times \vec{l}_2) \cdot \vec{l}_3 \quad (3.19)$$

However, the equation 3.20 is for the vector sides of the tetrahedron, and as mentioned previously, DioDe provides the vectors for an origin,

$$\begin{aligned} V &= \frac{1}{6}[(\vec{B} - \vec{A}) \times (\vec{C} - \vec{A})] \cdot \vec{A} \\ &= \frac{1}{6} \begin{vmatrix} B_x - A_x & B_y - A_y & B_z - A_z \\ C_x - A_x & C_y - A_y & C_z - A_z \\ A_x & A_y & A_z \end{vmatrix} \end{aligned} \quad (3.20)$$

where  $\vec{A}$ ,  $\vec{B}$  and  $\vec{C}$  are the vectors collected from DioDe.

### 3.3.3 Euler Characteristic

The Euler Characteristic,  $\chi$ , is a topological property related to

$$\chi = V - E + F, \quad (3.21)$$

Where  $V$  is the volume,  $E$  is the edge, and  $F$  is the face of the figure. However, by knowing the simplex complex,  $\chi$  can also be calculated with the following,

$$\chi = \sum_k^{\kappa} N_k (-1)^k \quad (3.22)$$

where  $N_k$  is the total amount of simplex in  $k$  dimension. Summing all the simplex dimensions (until the highest  $\kappa$ ) found in the data.

### 3.3.4 Mean Curvature

The last Minkowski functional to mention is the integral mean curvature,  $B$ . This calculates the total orientation of the surface. For instance, if we have lasagna, the curvature should be close to zero because of its wavelike shape; some regions will be positive while others negative, giving a net curvature approximated to zero.

$$B = \frac{1}{2\pi} \int_0^{2\pi} \kappa(\theta) d\theta \quad (3.23)$$

Where  $\kappa$  is the signed curvature for the respective  $\theta$ . The curvature is determined by the normal and the orientation triangle face. With DioDe, the first step to determine the curvature is to identify the normal of the triangle, which is given by the cross product of two vector sizes of the triangle or tetrahedron. Find the orientation of the normal, it requires the knowledge of the angle of these two vectors, which can be calculated with the following relation,

$$\cos(\gamma) = \frac{\vec{A} \times \vec{B}}{\|\vec{A} \times \vec{B}\|} \quad (3.24)$$

Where  $\gamma$  is the angle among  $\vec{A}$  and  $\vec{B}$ . The cotangent can determine the orientation of the triangle,

$$\cot(\gamma) = \frac{\cos(\gamma)}{\sin(\gamma)} \quad (3.25)$$

which is multiplied by the magnitude of the vectors,

$$\begin{aligned} \text{curv}_A &= \frac{\vec{B} - \vec{A}}{2} \cot(\gamma) \\ \text{curv}_B &= \frac{\vec{A} - \vec{B}}{2} \cot(\gamma) \end{aligned} \quad (3.26)$$

The orientation *curv* alongside the normal determines a single curvature, where the net curvature is the addition of the multiplication of the normal and curvature..

# Chapter 4

## Results

In this chapter, the first section illustrates NM simulations captured from LAMMPS visualized with OVITO, a visualization of molecular dynamics tool (VMD). The second section presents the optimization of the Minkowski functionals by varying  $\alpha$  and finalizing with the sought trend in the Euler Characteristic and Integral Mean Curvature graph.

### 4.1 Nuclear Matter Structures

For this research, the nuclear matter structures have densities,  $\rho$ , that range from  $0.02 \text{ fm}^{-3}$  to  $0.20 \text{ fm}^{-3}$  and are made of 2000 protons and 2000 neutrons. All the densities were simulated with an initial temperature of 4 MeV and a final temperature varying from 0.1 MeV to 1 MeV. The results present that for higher densities, the fight of the Coulomb and nuclear forces do not form nuclear pastas, and by defining the cutoff density as the highest density in which a nuclear pasta can be seen, the cutoff density decreases with higher final temperatures. In other words, there are fewer pasta phases for 1 MeV than for 0.1 MeV.

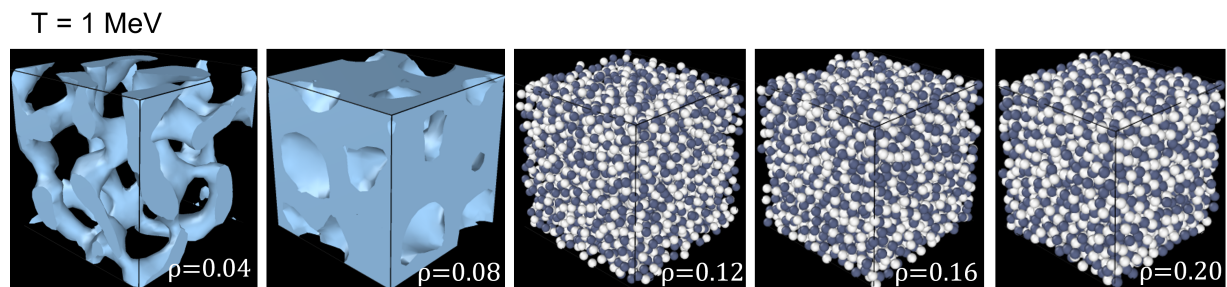


Figure 4.1: Nuclear matter structures for  $T = 1 \text{ MeV}$ .

In the figure 4.1 exists two nuclear pastas (that were simulated), where  $\rho = 0.04 \text{ fm}^{-3}$  is a waffle or jungle-gym, and  $\rho = 0.08 \text{ fm}^{-3}$  is anti-gnocchi. The densities above the anti-gnocchi pasta do not create a structure resembling pasta. By comparing all the simulations, the cutoff density in which pasta-like does not form resembles an anti-gnocchi pasta. The vast majority of the pastas were anti-gnocchi, where the lowest densities present a more symmetric feature. The highest densities have a few holes in their nuclear matter structure. This phenomenon is observed in  $T = 0.50 \text{ MeV}$ , three anti-gnocchi pastas are present, and in the latter, there exists an observable hole 4.2. The remaining nuclear matter simulations are in Appendix A.

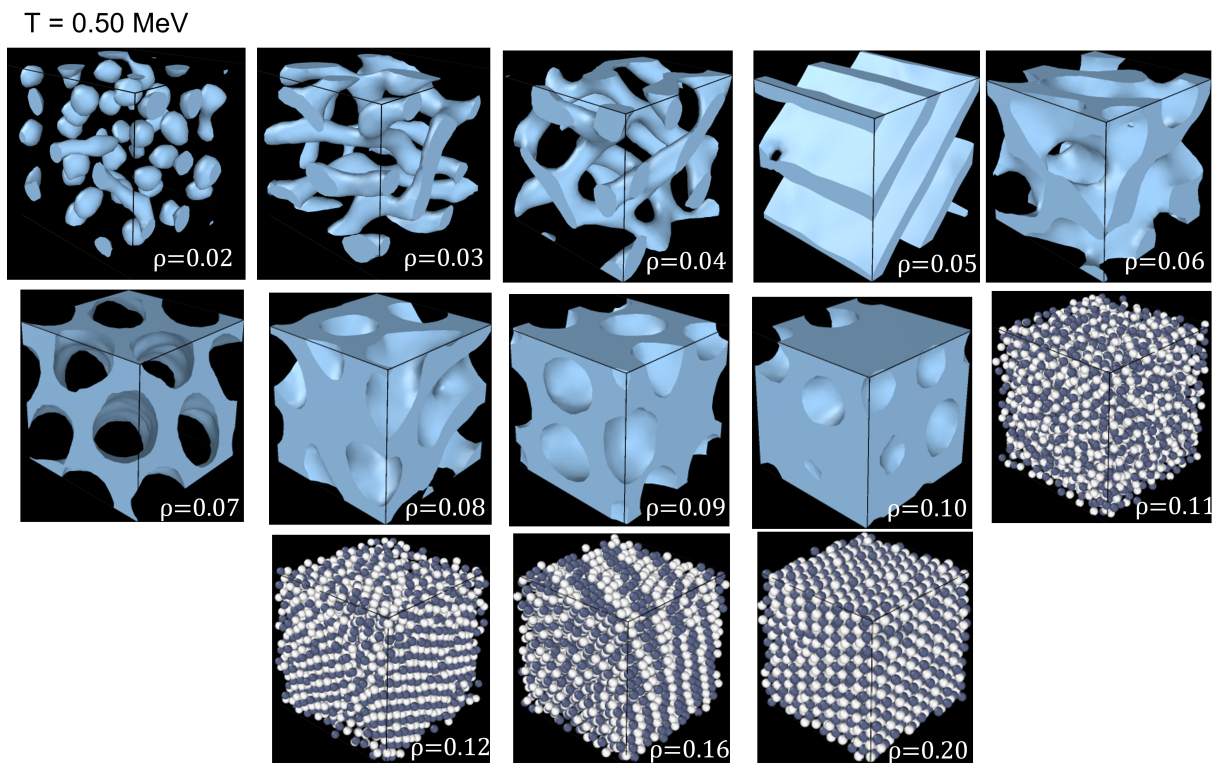


Figure 4.2: Nuclear matter structures for  $T = 0.50 \text{ MeV}$ .

Moreover, the nuclear matter transitions from 4 MeV to  $T_f$  can be analyzed through the caloric curve, which is a temperature-excitation energy correlation, because they belong to the first-order liquid-gas phase [1]. The caloric curve (fig. 4.3) connects the cooling system's

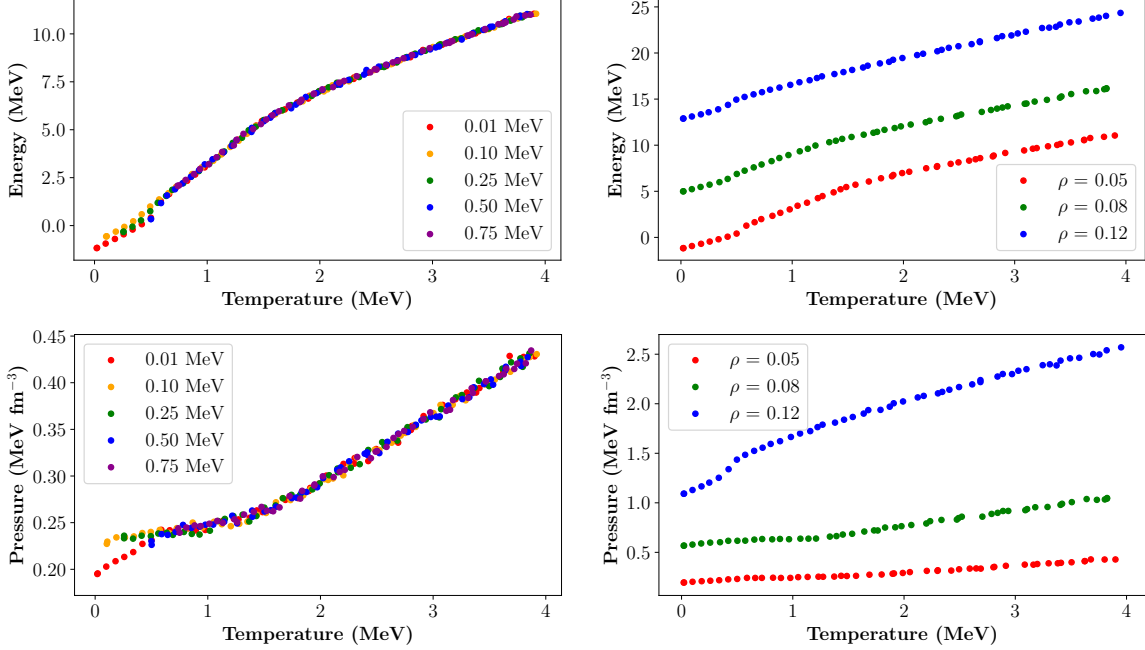


Figure 4.3: Energy and pressure as function of the temperature (leftmost) at  $\rho = 0.05$   $\text{fm}^{-3}$ , and (rightmost) at  $\rho=0.05, 0.08,$  and  $0.12$   $\text{fm}^{-3}$ .

temperature to the added energy required to reach  $T_f$ . In figure 4.3 for  $E(T)$ , it can be observe the phase shifts that are present on the discontinuities around  $T = 0.5$  MeV, and less noticeable, 2 MeV. The discontinuities match previous results that used molecular dynamics as a model [1]. A phase shift is produced because the energy that flows into the system is employed in non-thermal means, like breaking bonds while melting a crystal.

In general, the molecular dynamics simulations were able to reproduce pastas like gnocchi, spaghetti, lasagna, waffles, or defects, and the anti-pastas like anti-gnocchi and anti-spaghetti. Also, by observation, some of the structures were considerably hard to determine because they presented a combination of two types of pastas, which later were categorized as transitory pastas. Its name is because the surrounding densities of the transitory pastas have one of the two pastas. The nuclear matter structures that did not resemble any category of the nuclear pastas are referred to as nuclear matter or non-pastas. Figure 4.4 illustrates the visualizations on VMD for structures with different temperatures and



densities. Where a-d is lasagna-like, and e-h is an anti-gnocchi.

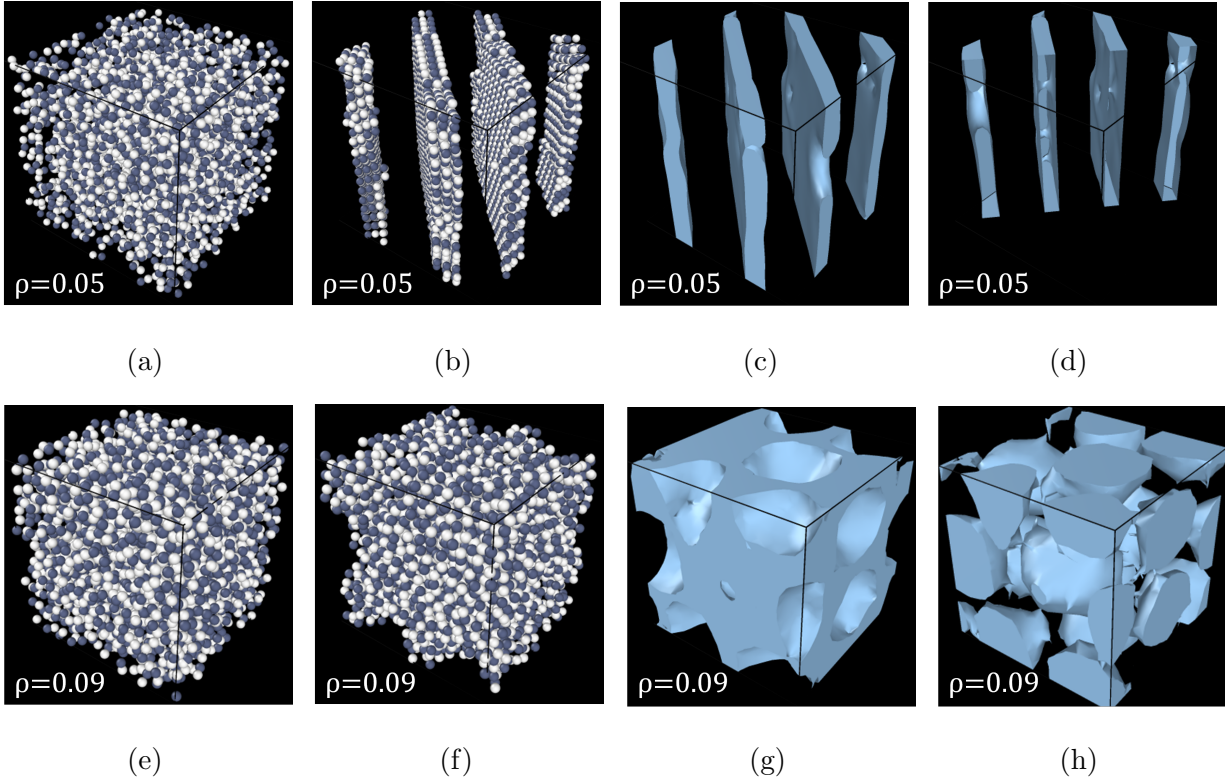


Figure 4.4: Diagram illustrating lasagna and anti-gnocchi pastas. (a) and (e) at 4 MeV; (b) and (f) at  $T=0.01$  MeV, and 0.50 MeV, respectively. While (c) and (g) implement the constructed surface mesh from OVITO, (d) slices (c) and (h) fill the void regions of (g).

## 4.2 Minkowski Functionals

Hereafter, the accuracy of the Minkowski functionals will depend on the chosen  $\alpha$ , which requires refinement before using the Euler-Curvature graph. From where it determines the pasta classification. The optimized results depend on analyzing the Minkowski functionals individually by giving a wide range of  $\alpha$ s and identifying the radius that produces concave and convex hulls. The concave hull is expected for lower  $\alpha$ 's because, within the pasta cluster, an  $\alpha$  that is short enough cannot have a particle A with a particle B touching that

are members of the same cluster. In contrast,  $\alpha$  is large enough to intersect with a particle from a neighboring cluster for the convex hull.

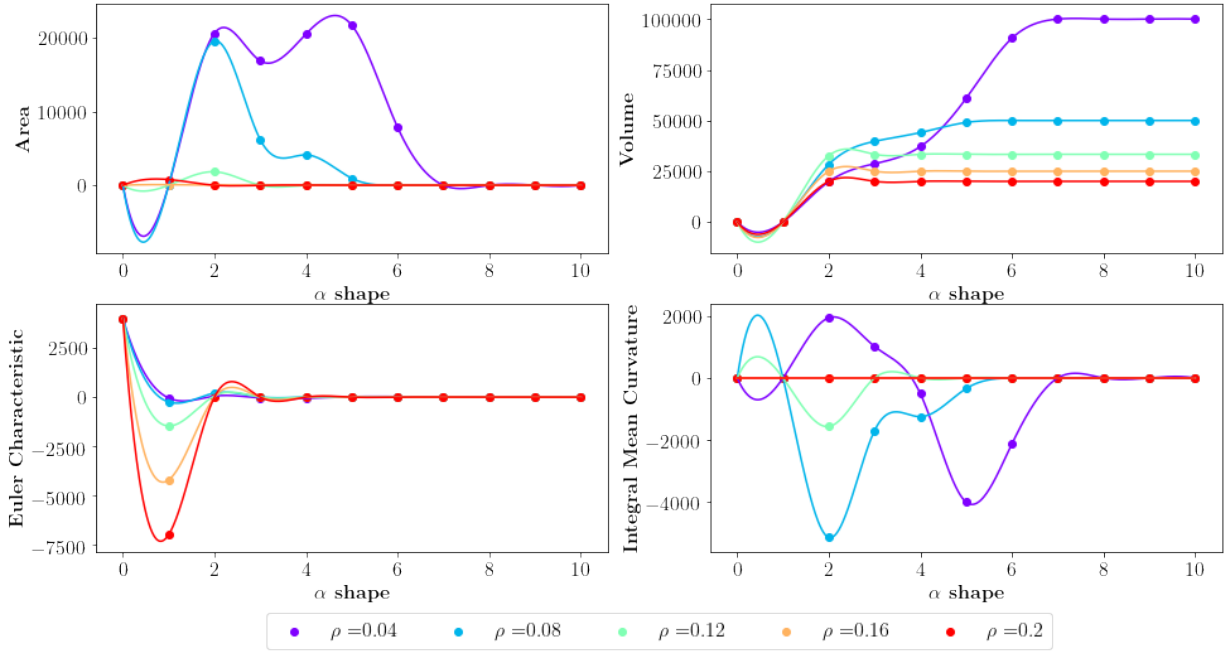


Figure 4.5: Minkowski functionals for  $T = 1$  MeV with  $0 < \alpha < 10$ , and density from 0.2 to  $0.2 \text{ fm}^{-3}$

Then, the optimization requires multiple steps; the first step is to identify the range in which the  $\alpha$  is a convex hull. The next step is to find a constant volume until  $\alpha$  interacts with a neighboring cluster. However, a constant volume is hard to recognize due to the multiple shapes a nuclear pasta can be (if it is pasta). For example, if  $\alpha$  varies from zero to ten, the constant volume cannot be appreciated in the nuclear matter for 1 MeV (fig. 4.5). However, for the temperature 0.01 MeV is more appreciable in figure 4.6 around the lengths  $2 < \alpha < 4$ .

Another parameter to consider is density. It affects a collapse in the Minkowski functionals for shorter and greater  $\alpha$ 's. For the nuclear structures with a higher density, their optimized  $\alpha$  is shorter compared to the lower densities because they are prone to convex. For example,  $\rho > 0.12 \text{ fm}^{-3}$  have constant volumes sooner than the lower densities, more-

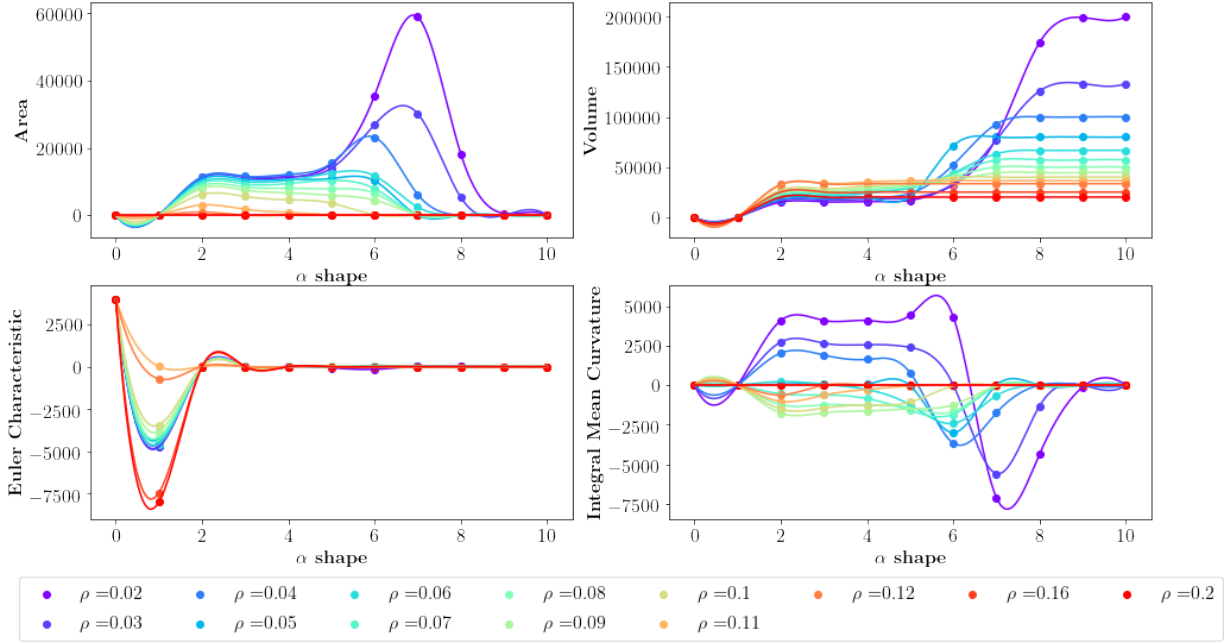
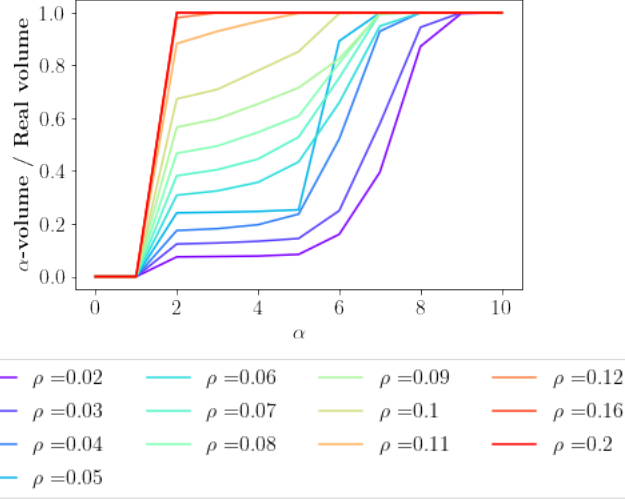


Figure 4.6: Minkowski functionals for  $T = 0.1$  MeV with  $0 < \alpha < 10$ , and density from  $0.2$  to  $0.2 \text{ fm}^{-3}$

over,  $\rho = 0.02 \text{ fm}^{-3}$  is the last nuclear pasta to collapse (gnocchi). The gnocchi structure takes longer to collapse, and multiple constant volumes can be seen that look like steps, which is better appreciated in the normalization of the volume (fig. 4.7).

The normalization of the volume proves that DioDe is designed to have a maximum volume proportional to the box conditions because for  $\alpha = 10^5$  the volume remains constant, equivalent to  $\alpha = 10$ . Moreover, the superficial area becomes zero once the maximum volume is archived, indicating that the area is equivalent to the box faces. Furthermore,  $\chi$  and  $B$  will tend to zero as no superficial area exists to measure. Consequently, the convex hull is defined for  $\alpha$ 's that gives the box volume and for a zero superficial area, giving  $\chi$  and  $B$  equal to zero. Moreover, determining the Minkowski functionals must consider that  $\alpha$  can fall into a concave hull, and the optimization requires refinement.



centerline

Figure 4.7: Volume normalization for  $T = 0.01 \text{ MeV}$  and  $0.02 \text{ fm}^{-3} < \rho < 0.20 \text{ fm}^{-3}$ , where unity is equivalent to a volume with box dimensions.

### 4.2.1 Dictate Level of Refinement

The refinement procedure must find the concave hull limit by reducing the intervals of  $\alpha$  and closely observe the Minkowski functionals. Once the concave hull limit is identified, and the Minkowski functionals are ideal, it is stated that for  $\alpha_r$ . The concave hull in the volume behaves as a steeper slope for the volume change, and  $\alpha_r$  is for the volume, which approximately has a constant slope. For the superficial area, the concave hull is identified as a maximum. The refined superficial area has a specific number of simplex-3 (tetrahedrons); however, for a shorter  $\alpha$  some simplex-3 may be counted as simplex-2, which calculates the higher surface area.

More importantly,  $\chi$  is the variable that pinpoints  $\alpha_r$ . Whereas the volume and superficial area behave by the analysis, the multiple pastas have a slight complication in finding this constant parameter. However,  $\chi$  is a topological tool, and independent of the size, its topology remains constant. In brief, the refinement process is accomplished by first optimizing an  $\alpha$  range, then locating a maximum area followed by an approximated constant increasing volume. After that range, look for  $\chi$  constant by optimizing the Minkowski

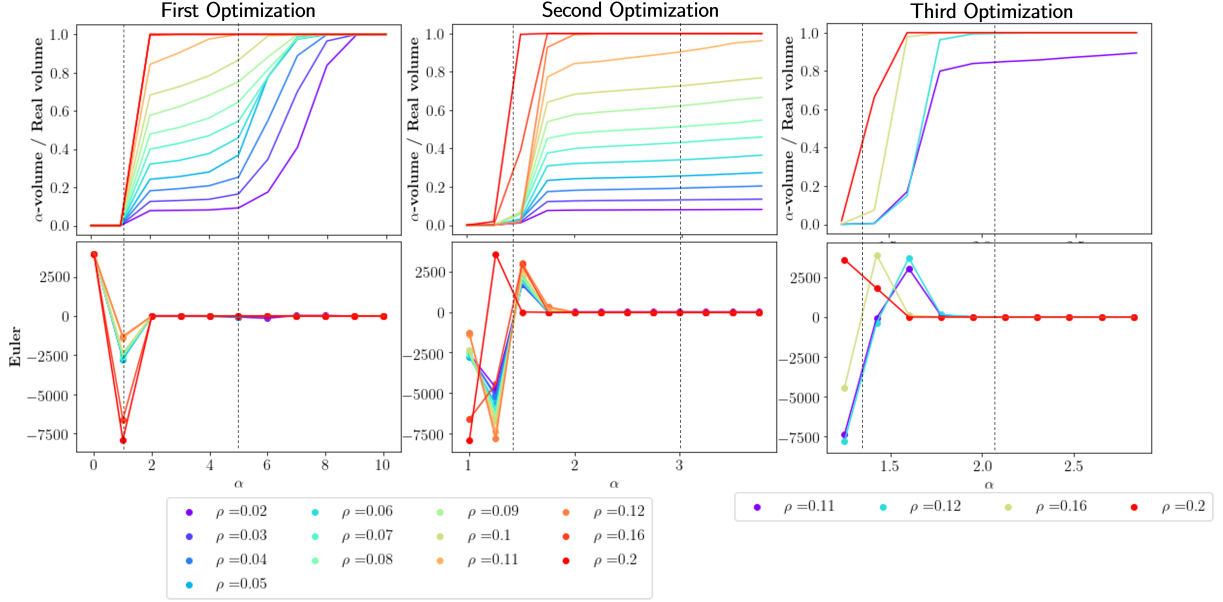


Figure 4.8: Illustration of the volume normalization, and  $\chi$  for three optimizations of the  $\alpha$  for  $T = 0.25$  MeV.

functionals. At the same time, the non-pastas require a third optimization caused by their non-pasta shape. As mentioned above, the greater densities are prone to the convex hull and small jump from the concave to the convex hull. Then, with a third optimization,  $\alpha_r$  is found for a more specific value, in which  $\chi$  is constant and should be closer to zero (no-holes).

In figure 4.8, the gray dotted line indicates the observed region for three relevant optimizations. In the first optimization,  $\alpha$  varied from 0 to 10 for the normalized volume and  $\chi$ , and the region in the gray dotted space is the emphasized region for the second optimization, and those values that were hard to determine, such as the non-pasta structure, required a third optimization. Most non-pasta structures have  $\chi$  proportional to zero because the particles are organized in a structure without holes.

### 4.2.2 Relation $\chi$ , and $B$

Once the nuclear structures were analyzed, the non-pasta structures were removed from the trend identification. Either their particle occupied most of the box volume, and DioDe visualized those structures as a convex hull with outputs such as  $\chi = 0$ ,  $S = 0$ , and  $B = 0$  or they were unable to optimize.

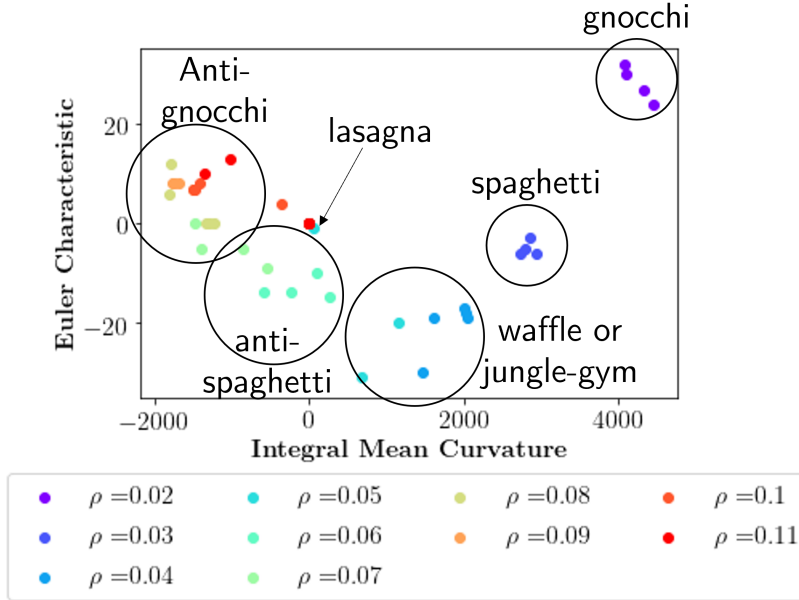
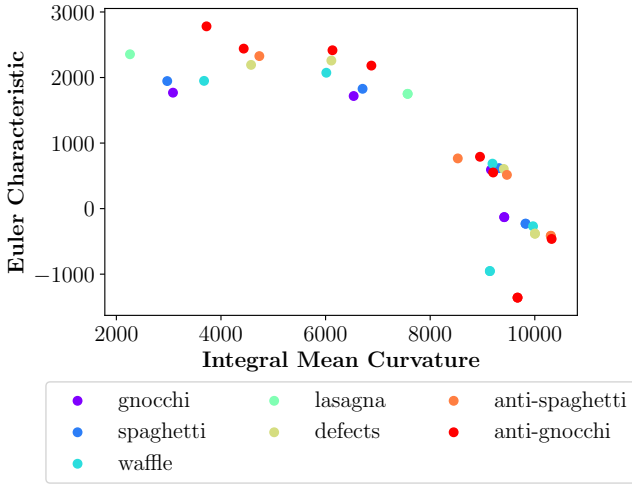


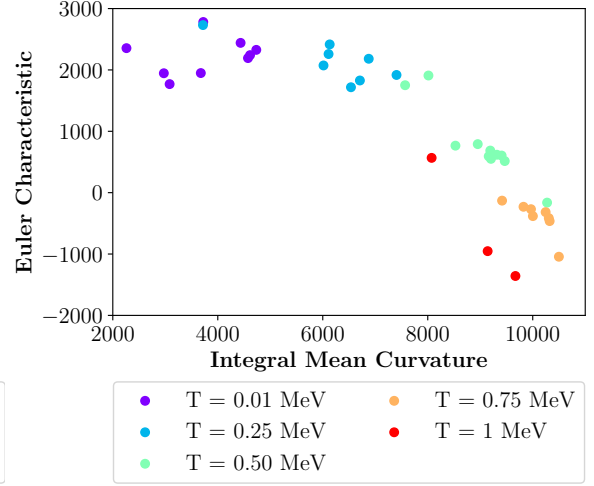
Figure 4.9: Euler Characteristic *versus* Curvature graph for optimized  $\alpha$ .

The last item to visualize is  $B$  *versus*  $\chi$  graph (fig. 4.9). A trend could be identified with the density; it flows in the clockwise direction and finalizes with the cutoff pasta (anti-gnocchi). After that, the non-pasta will tend to zero. The lasagna is an exception to the trend; it had small curvature compared to the other pastas, and their  $\chi$  is almost proportional to zero (if the structure does not have a perforation on it like for 0.50 MeV). Furthermore, the pastas are located in the positive curvature region and the anti-pastas in the negative region. Besides, the pastas with a more complex structure are expected to have a more negative  $\chi$  than sphere-like structures. For instance, gnocchi and anti-gnocchi have a more positive value than spaghetti and jungle gym and their respective anti-pastas.

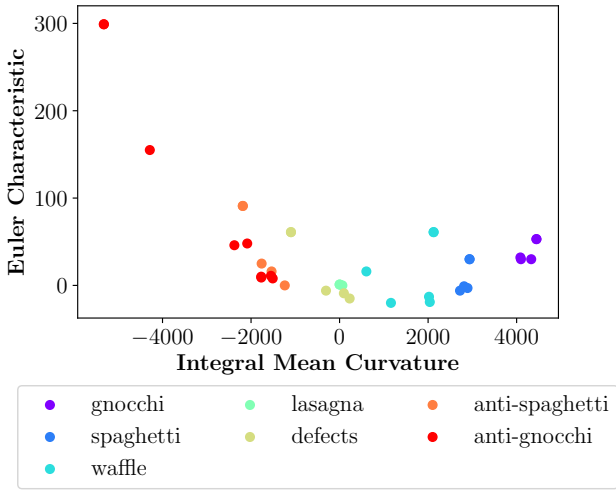
Moreover, suppose the pastas were visualized with a non-refined  $\alpha$ , which did not belong to either the convex or concave hull. In that case, the pattern persists, except that lasagnas are no longer equivalent to zero. Figure 4.10 shows  $\alpha = 1.5$  in which most of their structures landed in the parameter of concave hull region, and  $\alpha = 2.0$  most were not concave and were selected by visualizing the volume that increased slowly proportionally to  $\alpha$ . For  $\alpha = 2.0$ , the trend flows in the clockwise direction, and the pastas that almost became non-pastas (some anti gnocchi) had the highest  $\chi$ .



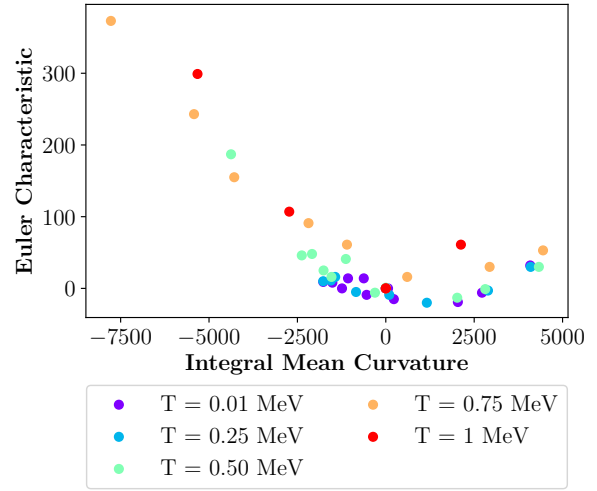
(a)



(b)



(c)



(d)

Figure 4.10: Euler-Curvature relation for (a-b)  $\alpha = 1.5$ , and (c-d)  $\alpha = 2.0$ .



# Chapter 5

## Conclusions

The  $\alpha$  shape model can measure the Minkowski functionals of nuclear pastas, in which a trend is found. The trend simplifies the classification of nuclear pastas when a surface construction tool is not provided in the visualization tool. It suffices for various nuclear pastas, including gnocchi, spaghetti, jungle gym, defects, and their anti-pastas. Furthermore, the  $\alpha$  model struggles to measure the nuclear matter structures that did not produce nuclear pastas. By neglecting the non-pasta forms, the Euler Characteristic and Curvature graph trend flows in the clockwise direction. The pattern persists for non-optimized  $\alpha$  radius as long as the length does not fall in the concave or convex hull.

The  $\alpha$ 's optimization may be accomplished by observing the Minkowski functionals for a range of  $\alpha$  and, mainly, finding a constant  $\chi$ . The main difference when the  $\alpha$  is not optimized from a refined value is that in the Euler *versus* Curvature graph, the lasagnas are in the origin because their wavy curvature gives a net sum close to zero, but the trend persists. Moreover, when the lasagna pastas do not present holes in their structure, computing a  $\chi = 0$ . On the other hand, anti-pastas have negative curvature, and pastas have positive curvature, and  $\chi$  gives the complexity of the structure; for simple systems like gnocchi and anti-gnocchi,  $\chi$  has the most significant values. At the same time, structures with more complex (intersecting slob) have a lower  $\chi$  independently of their optimized  $\alpha$ .

Furthermore, nuclear matter structures for higher final temperatures have fewer pasta structures than cooler ones. It was found that the last nuclear pasta to appear was the anti-gnocchi for higher densities, and the symmetry of the structure disappeared. From the simulations, none of a single temperature could generate a pasta for density above  $0.12 \text{ fm}^{-3}$ . With the  $\alpha$  shapes model, the anti-gnocchi pastas almost considered non-pastas had

properties close to the convex hull.

The optimized results indicated that those that are non-pastas tend to disrupt the clockwise trend. In conclusion, the pastas follow a clockwise direction, and the greatest  $\chi$  values belong to the gnocchi or anti-gnocchi pastas. Meanwhile, positive curvature is equivalent to pastas, and negative curvature to anti-pastas.

With this method, future work could be to determine two kinds of pasta from a molecular dynamics' simulation in the analysis of nuclear pasta. The nuclear structure must contain a variable density in the system instead of a fixed density, and it is expected that a transition could be found. Moreover, more structures must be analyzed, including the asymmetrical conditions in which the number of protons is not equivalent to the number of neutrons, multiple final temperatures, and, as mentioned before, a variable density in the initial conditions.

# References

- [1] J., A., López, C. O. Dorso and G., Frank, “Properties of nuclear pastas”, *Frontiers of Physics*, 2021, Vol. 16, No. 2, pp. 24301.
- [2] B. W. Carroll and D. A. Ostlie, *An introduction to modern astrophysics*, Cambridge University Press, 2017.
- [3] L. Bao-An, “Tasting nuclear pasta made with classical molecular dynamics simulations”, *Frontiers of Physics*, 2021, Vol. 16, No.2, pp. 24302
- [4] C. O. Dorso, P. A. Giménez Molinelli and J. A. López, “Topological characterization of neutron star crusts”, *Physical Review C*, 2012, Vol. 86, No. 5.
- [5] A. R. Choudhuri, *Astrophysics for Physicists*, Cambridge University Press, 2010.
- [6] R. Shafieepour, H. R. Moshfegh and J. Piekarewicz, “Characterization of the inner edge of the neutron star crust”, *arXiv:2201.02429 [nucl-th][Preprint]*. January 7, 2022 [cited 2022 Feb 13].
- [7] D. Frenkel and B. Smit, *Understanding Molecular Simulation: From Algorithms to Applications*, Academic Press, 2002.
- [8] Delaunay, Boris (1934). ”Sur la sphère vide”. Bulletin de l’Académie des Sciences de l’URSS, Classe des Sciences Mathématiques et Naturelles. 6: 793–800.
- [9] Edelsbrunner, H.: The union of balls and its dual shape. In: 9th Annual Symposium on Computational Geometry, pp. 218–231 (1993)
- [10] Edelsbrunner, H., Facello, M.A., Liang, J.: On the definition and the construction of pockets in macromolecules. *Discrete Appl. Math.* 88, 83–102 (1998)

- [11] Edelsbrunner, H.: Surface reconstruction by wrapping finite point sets in space. *Discrete Comput. Geom.* 32, 231–244 (2004)
- [12] Amenta, N., Bern, M.: Surface reconstruction by Voronoi filtering. *Discrete Comput. Geom.* 22, 481–504 (1999)
- [13] D. Morozov, “Alpha shapes”, <https://mrzv.org/tmp/alpha-shapes.pdf>.
- [14] Amenta, N., Choi, S., Dey, T.K., Leekha, N.: A simple algorithm for homeomorphic surface reconstruction. In: 16th Annual ACM Symposium on Computational Geometry, pp. 213–222 (2000)
- [15] M. Petitjean, “Spheres Unions and Intersections and Some of their Applications in Molecular Modeling,” in: A. Mucherino, C. Lavor, L. Liberti and N. Maculan (eds.), *Distance Geometry: Theory, Methods, and Applications*, Springer, New York, 2013, pp. 61–83.
- [16] A. P. Thompson, H. M. Aktulga, R. Berger, D. S. Bolintineanu, W. M. Brown, P. S. Crozier, P. J. in ’t Veld, A. Kohlmeyer, S. G. Moore, T. D. Nguyen, R. Shan, M. J. Stevens, J. Tranchida and C. Trott and S. J. Plimpton, “LAMMPS - a flexible simulation tool for particle-based materials modeling at the atomic, meso, and continuum scales,” *Comp. Phys. Comm.*, 2022, Vol. 271, pp. 108171.
- [17] F. Ji, J. Hu and H. Shen, “Nuclear pasta and symmetry energy in the relativistic point-coupling model”, *Physical Review C*, 2021, Vol. 103, No. 5.
- [18] J. F. Acevedo, J. Bramante, R. K. Leane and N. Raj, “Warming nuclear pasta with dark matter: kinetic and annihilation heating of neutron star crusts”, *Journal of Cosmology and Astroparticle Physics* 2020, Vol. 2020, No. 03, pp. 038–038.
- [19] M. E. Caplan, A. S. Schneider and C. J. Horowitz, “The Elasticity of Nuclear Pasta”, *Physical Review Letters*, 2018, Vol. 121, No. 13.

- [20] W. G. Newton, S. Cantu, S. Wang, A. Stinson, M. A. Kaltenborn, J. R. Stone, “Glassy quantum nuclear pasta in neutron star crusts”, *Phys. Rev. C*, 2022, Vol. 105, No. 2, pp. 025806.
- [21] H. Pais, S. Chiacchiera and C. Providência, “Light clusters, pasta phases, and phase transitions in core-collapse supernova matter”, *Phys. Rev. C*, 2015, Vol. 91, No. 5, pp. 055801.
- [22] M. Oertel, M. Hempel, T. Klähn and S. Typel, “Equations of state for supernovae and compact stars”, *Rev. Mod. Phys.*, 2017, Vol. 89, No. 1, pp. 015007.
- [23] A. W. Steiner, S. Gandolfi, F. J. Fattoyev and W. G. Newton, “Using neutron star observations to determine crust thicknesses, moments of inertia, and tidal deformabilities”, *Phys. Rev. C*, 2015, Vol. 91, No. 1, pp. 015804.
- [24] S. S. Avancini, C. C. Barros, Jr., D. P. Menezes, and C. Providencia, *Physical Review C* 82, 025808 (2010)
- [25] T. Maruyama, T. Tatsumi, D. N. Voskresensky, T. Tanigawa, and S. Chiba, *Physical Review C* 72, 015802 (2005).
- [26] O. L. Caballero, S. Postnikov, C. J. Horowitz, and M. Prakash, *Physical Review C* 78, 045805 (2008).
- [27] D. P. Menezes, S. S. Avancini, C. Providencia, and M. D. Alloy, in *Neutron Star Crust*, edited by C. A. Bertulani and J. Piekarewicz (Nova Science, Hauppauge, NY, 2012).
- [28] G. Watanabe, H. Sonoda, T. Maruyama, K. Sato, K. Yasuoka, and T. Ebisuzaki, *Phys. Rev. Lett.* 103, 121101 (2009).
- [29] C. J. Horowitz, *Eur. Phys. J. A* 30, 303 (2006).

- [30] H. Sonoda, G. Watanabe, K. Sato, K. Yasuoka, and T. Ebisuzaki, *Physical Review C* 81, 049902(E) (2010).
- [31] A. S. Schneider, C. J. Horowitz, J. Hughto and D. K. Berry, “Nuclear pasta formation”, *Physical Review C*, 2013, Vol. 88, No. 6.
- [32] J. D. Gardiner, J. Behnsen and C. A. Brassey, “Alpha shapes: determining 3D shape complexity across morphologically diverse structures”, *BMC evolutionary biology*, 2018, Vol. 18, No. 1, pp. 1-16.
- [33] R. van de Weygaert, E. Platen, G. Vegter, B. Eldering and N. Kruithof, “Alpha Shape Topology of the Cosmic Web” *2010 International Symposium on Voronoi Diagrams in Science and Engineering*, 2010, pp. 224-234
- [34] J. A. López and C. Dorso, *Lectures Notes on Phase Transformations in Nuclear Matter*, World Scientific, 2000.
- [35] A. Barranón, R. Cardenas, C. O. Dorso and J. A. López, “The critical exponent of nuclear fragmentation” *Acta Physica Hungarica Series A, Heavy Ion Physics*, 2003, Vol. 17, No. 1, pp. 59–73.
- [36] P.A. Giménez Molinelli, J.I. Nichols, J.A. López b, C.O. Dorso, Simulations of cold nuclear matter at sub-saturation densities, *Nuclear Physics A* 923 (2014) 31–50.
- [37] <https://www.nersc.gov/>
- [38] <https://www.ovito.org/>

# Appendix A

## Results: Nuclear Pasta structures

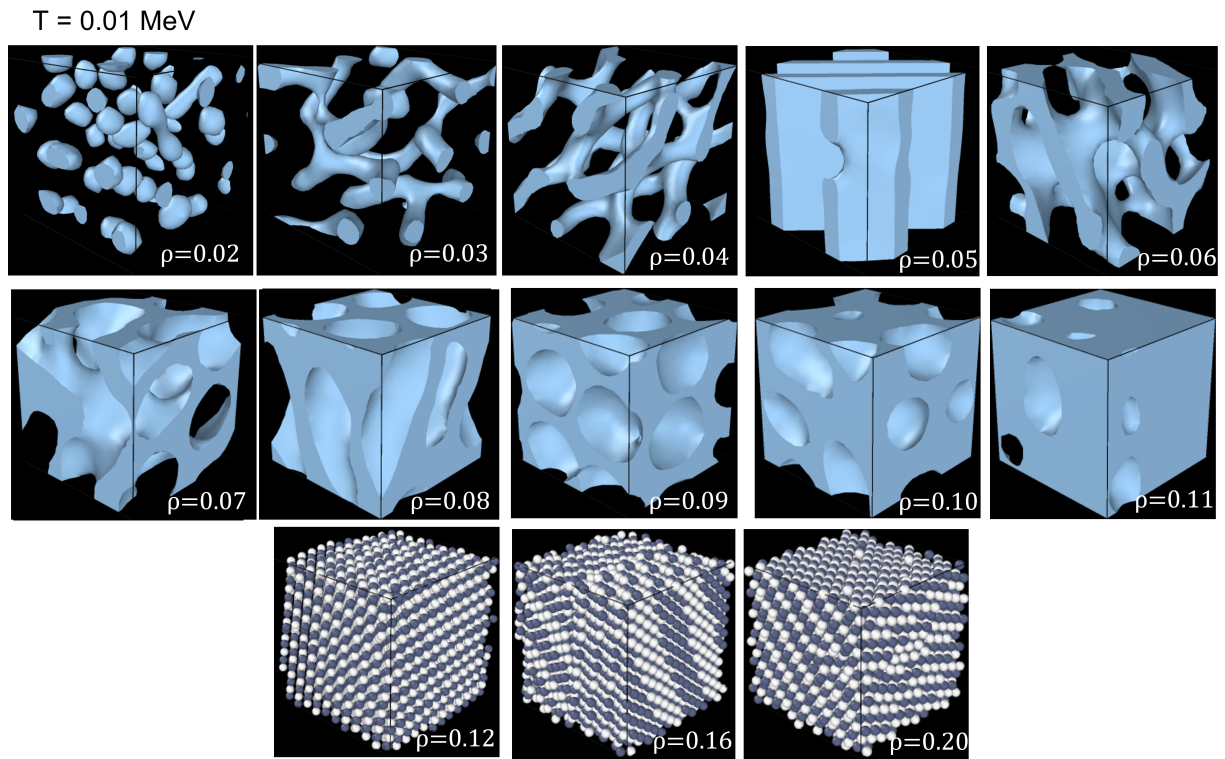


Figure A.1: Nuclear matter structures for  $T = 0.01 \text{ MeV}$ .

T = 0.25 MeV

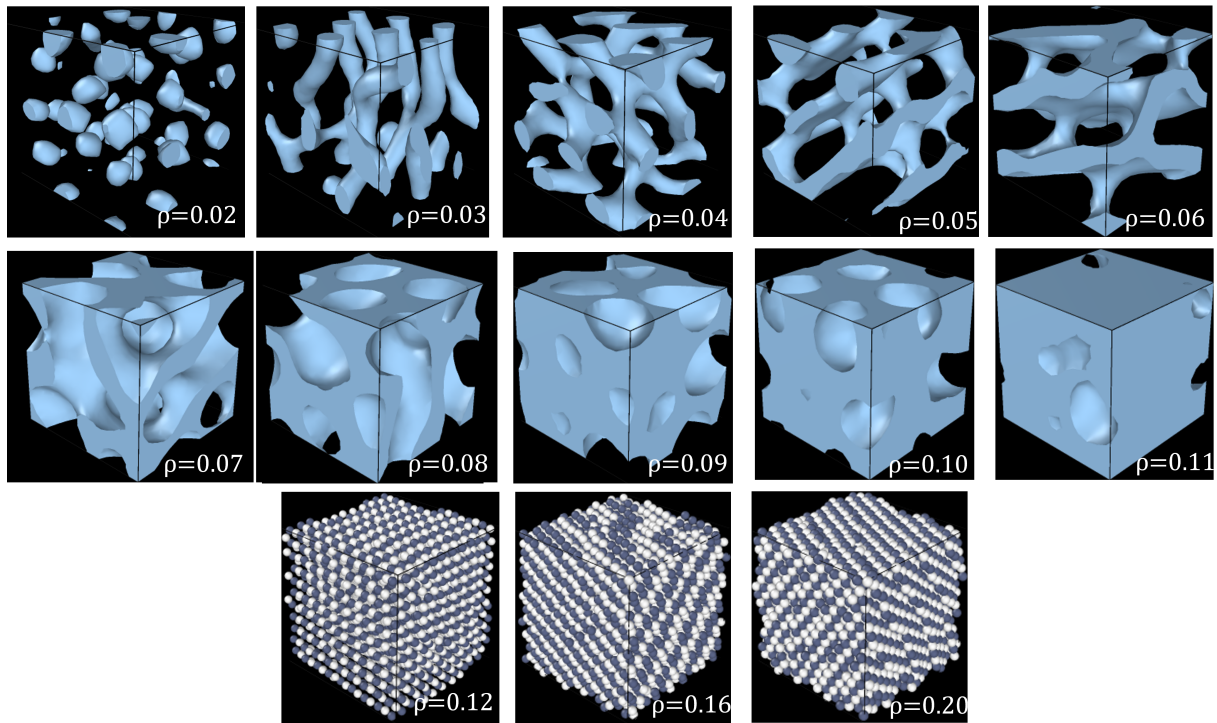


Figure A.2: Nuclear matter structures for  $T = 0.25$  MeV.



T = 0.50 MeV

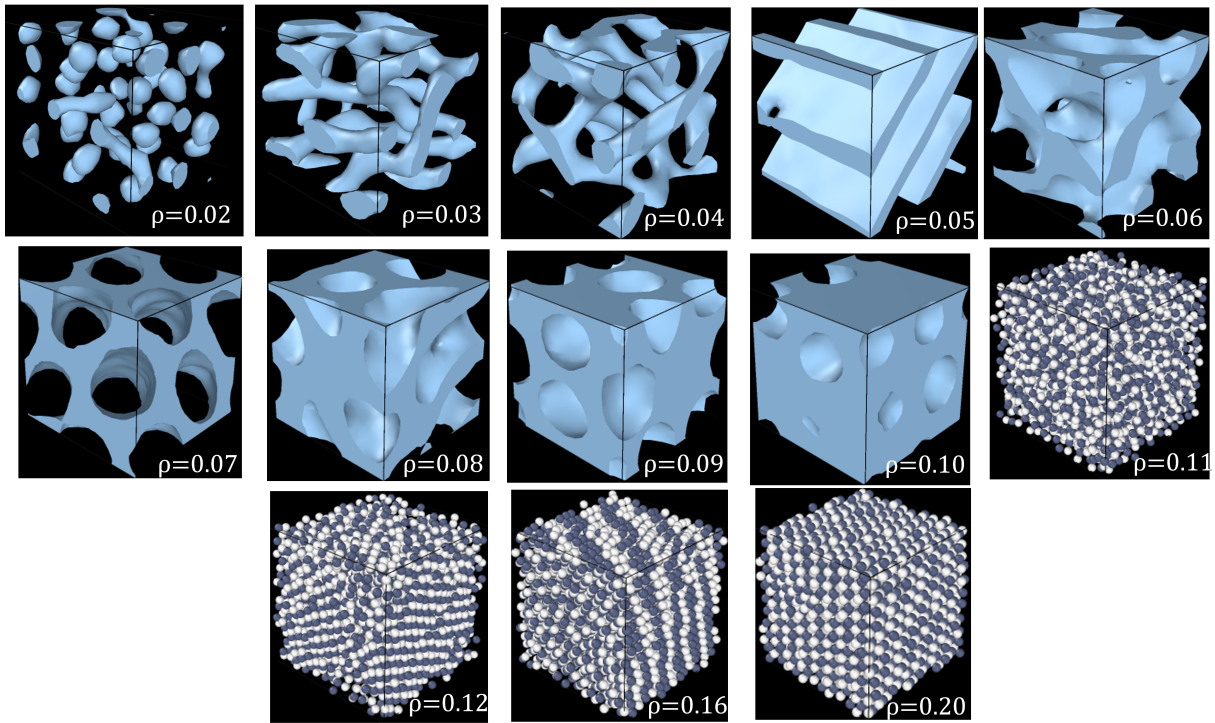


Figure A.3: Nuclear matter structures for T = 0.50 MeV.

T = 0.75 MeV

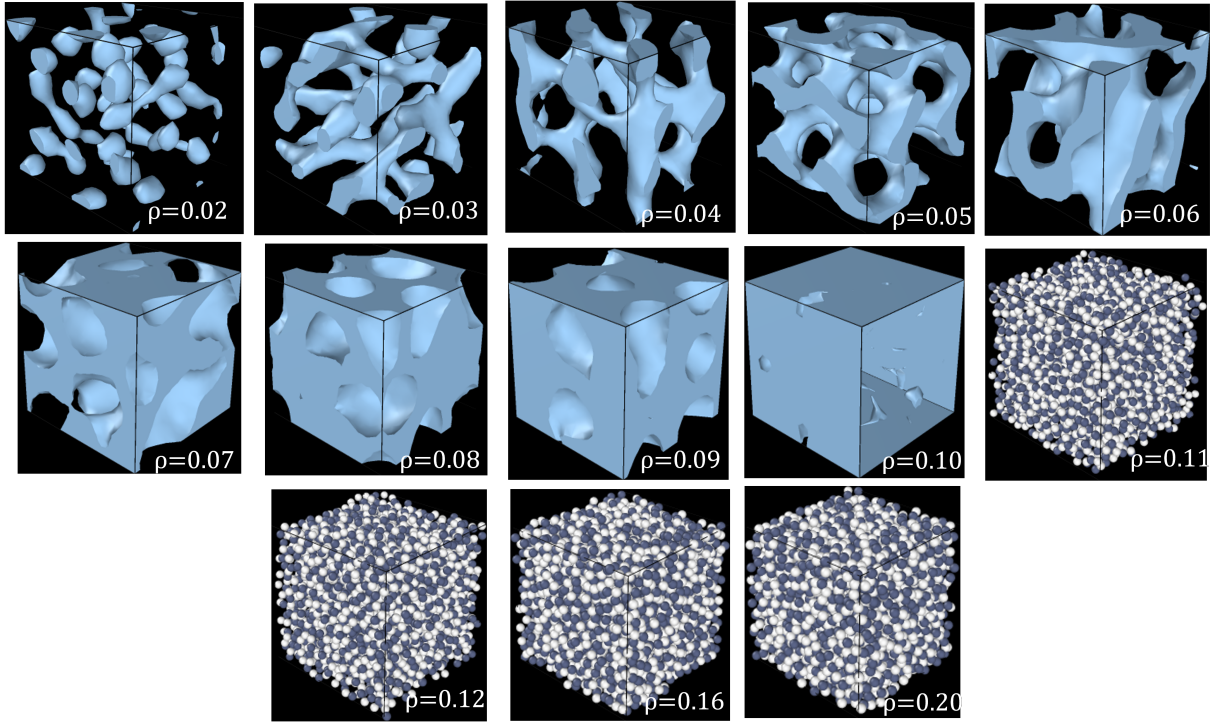


Figure A.4: Nuclear matter structures for T = 0.75 MeV.

T = 1 MeV

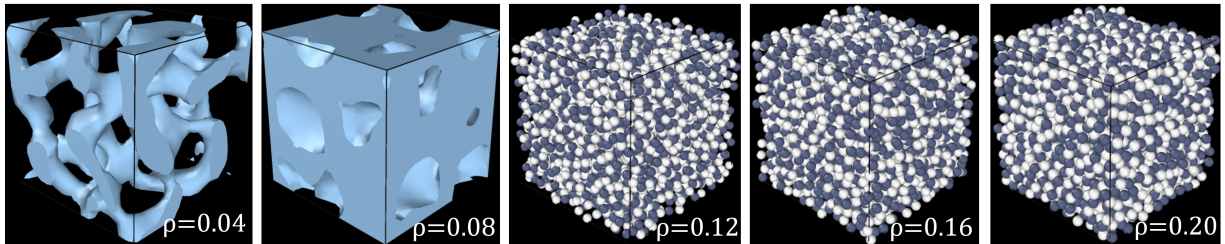


Figure A.5: Nuclear matter structures for T = 1 MeV.

# Appendix B

## Table

Table B.1: Classification Curvature - Euler from [4].

| Density<br>( $fm^{-3}$ ) | Curvature | Euler | $x = 0.5$<br>Topology            |
|--------------------------|-----------|-------|----------------------------------|
| 0.01                     | (a) 100   | 100   | Gnocchi                          |
| 0.015                    | 73        | 50    | Gnocchi                          |
| 0.018                    | 58        | 17    | Gnocchi - Spaghetti              |
| 0.021                    | 36        | -25   | Spaghetti - Jungle gym           |
| 0.024                    | 22        | -28   | Spaghetti - Jungle gym           |
| 0.027                    | 9         | -42   | Jungle gym - Lasagna             |
| 0.03                     | 10        | -39   | Jungle gym - Lasagna             |
| 0.033                    | 9         | -47   | Jungle gym                       |
| 0.036                    | 8         | -42   | Jungle gym                       |
| 0.039                    | -11       | -6    | Lasagna - Anti jungle gym        |
| 0.042                    | -15       | -8    | Lasagna - Anti jungle gym        |
| 0.045                    | 1         | -33   | Lasagna - Jungle gym             |
| 0.048                    | -5        | -11   | Lasagna                          |
| 0.051                    | -7        | -17   | Anti-Spaghetti - Anti jungle gym |
| 0.054                    | -1        | -11   | Lasagna - Anti jungle gym        |
| 0.057                    | -9        | -30   | Anti jungle gym                  |
| 0.06                     | -9        | -17   | Anti jungle gym                  |
| 0.063                    | -10       | -30   | Anti jungle gym                  |
| 0.072                    | -12       | -8    | Anti Spaghetti -Anti jungle gym  |
| 0.084                    | (t) -19   | -8    | Anti jungle gym                  |

# Curriculum Vitae

Daniela Ramirez Chavez was born on September 3rd, 1997. She graduated from Universidad Autonoma de Ciudad Juarez in the fall of 2020, last year well-known for COVID 19, and had an internship at Texas State University - San Marcos in the fall 2019. She received her bachelor's degree in Engineering Physics, and in the spring of 2021, she entered to the Graduate School of The University of Texas at El Paso.

Throughout the year, she worked as a Graduate Teacher Assistant, and on her last year, as well, she participated in TREND fellowship (Texas Research Expanding Nuclear Diversity) remotely and in-site during the summer of 2022 at the Cyclotron Institute located at Texas A&M University, College Station, TX.

Permanent address: 7116 Ramada Drive,  
El Paso, TX 79912-4927